

# Electronic coarse-graining of long conjugated molecules: Case study of non-fullerene acceptors

Cite as: J. Chem. Phys. 159, 024107 (2023); doi: 10.1063/5.0155488

Submitted: 20 April 2023 • Accepted: 21 June 2023 •

Published Online: 10 July 2023



View Online



Export Citation



CrossMark

Andriy Zhugayevych,<sup>a)</sup> Kun-Han Lin, and Denis Andrienko<sup>b)</sup>

## AFFILIATIONS

Max Planck Institute for Polymer Research, Ackermannweg 10, 55128 Mainz, Germany

<sup>a)</sup>Author to whom correspondence should be addressed: [andriy.zhugayevych@mpip-mainz.mpg.de](mailto:andriy.zhugayevych@mpip-mainz.mpg.de)

<sup>b)</sup>Electronic mail: [denis.andrienko@mpip-mainz.mpg.de](mailto:denis.andrienko@mpip-mainz.mpg.de)

## ABSTRACT

By considering only one electronic state per molecule, charge transport models of molecular solids neglect intramolecular charge transfer. This approximation excludes materials with quasi-degenerate spatially separated frontier orbitals, such as non-fullerene acceptors (NFAs) and symmetric thermally activated delayed fluorescence emitters. By analyzing the electronic structure of room-temperature molecular conformers of a prototypical NFA, ITIC-4F, we conclude that the electron is localized on one of the two acceptor blocks with the mean intramolecular transfer integral of 120 meV, which is comparable with intermolecular couplings. Therefore, the minimal basis for acceptor–donor–acceptor (A–D–A) molecules consists of two molecular orbitals localized on the acceptor blocks. This basis is robust even with respect to geometry distortions in an amorphous solid, in contrast to the basis of two lowest unoccupied canonical molecular orbitals notwithstanding only thermal fluctuations in a crystal. The charge carrier mobility can be underestimated by a factor of two when using single site approximation for A–D–A molecules in their typical crystalline packings.

© 2023 Author(s). All article content, except where otherwise noted, is licensed under a Creative Commons Attribution (CC BY) license (<http://creativecommons.org/licenses/by/4.0/>). <https://doi.org/10.1063/5.0155488>

## I. INTRODUCTION

Organic semiconductors constitute a broad class of functional materials for optoelectronic and energy applications.<sup>1</sup> Design of such materials requires an accurate description of their electronic properties,<sup>2–7</sup> with the most accurate models developed for molecular solids, such as pentacene<sup>8–10</sup> or naphthalene.<sup>11,12</sup> Despite these advances, modeling charge transport in molecular solids continues to pose challenges. In molecular crystals, conventional models, such as band transport or hopping transport, are not always appropriate.<sup>6</sup> The current state-of-the-art approach involves evolving the trajectory of charge carriers using surface hopping or other methods correctly describing electron–phonon interaction in organic semiconductors.<sup>8</sup> This is only feasible in a *coarse-grained electronic basis*: typically, with one molecular orbital (MO) per molecule, so that the electronic wave-function is approximated by a linear combination of such MOs.<sup>13</sup> In particular, the highest occupied molecular orbital (HOMO) is used for the hole transport, and the lowest unoccupied molecular orbital (LUMO) is used for the electron transport. Importantly, the coarse-grained basis is *fixed* in the same sense

as contracted Gaussian functions are fixed, and only translations and rotations of the entire MO are allowed. The robustness of this description relies on the energetic separation of HOMO/LUMO from the remaining MOs. This separation, typically more than 1 eV, ensures that the solid-state electronic bands composed of different MOs do not overlap. The rigidity of molecules makes the coarse-grained basis robust with respect to fluctuations in molecular geometries.

For large molecules, the energy separation between frontier MOs is comparable to both their vibrational broadening and intermolecular dispersion (a few tenths of eV), making the basis of one MO per molecule incomplete for a description of frontier MOs of molecular solids. If the molecule is rigid, such as polycyclic aromatic hydrocarbons, the simplest reasonable approximation is to include all quasi-degenerate MOs into the coarse-grained basis. In nonrigid molecules, however, geometry fluctuations under ambient conditions can be so large that MOs of one conformation are no longer representable on the basis of canonical MOs of another conformation. This case requires a more sophisticated electronic coarse-graining, which is the subject of this work. Specifically, we will

compare the accuracy of different coarse-grained bases in representing frontier orbitals of a nonrigid molecule subject to fluctuations of its geometry under typical conditions for organic semiconductors, mainly in a solid state. It should be noted that inaccurate electronic coarse-graining might result in not only a deficient basis but also a wrong intramolecular charge dynamics in the approximation of instantaneous transitions between degenerate electronic states, which is reasonable for such molecules as fullerenes.<sup>14</sup>

To perform a detailed investigation, we will consider the case study of the ITIC-4F molecule<sup>15</sup> whose bulk geometry in both crystalline and smectic phases is known.<sup>16</sup> ITIC-4F belongs to a class of high-performing non-fullerene acceptors (NFA),<sup>17</sup> majority of which have an acceptor–donor–acceptor (A–D–A) molecular architecture<sup>18–21</sup> (Fig. 1) with a large separation between the acceptor blocks, resulting in a quasi-degenerate LUMO.<sup>22</sup> The most appropriate approach for studying the influence of molecular fluctuations on the electronic structure would be an all-atom non-adiabatic molecular dynamics (MD).<sup>23</sup> However, it is computationally demanding for a reasonably sized cluster of NFA molecules, not talking about bulk solids.<sup>24</sup> To investigate structural models with thousands of atoms, such as amorphous ITIC-4F, alternative strategies must be adopted. Here, we sample molecular conformations using a computationally efficient approach: a combination of the classical MD with a force-field and classical/quantum harmonic oscillator models with vibrational modes calculated using density functional theory (DFT). A statistical analysis of electronic states using single-point electronic structure calculations can then be performed based on the sampled structures. At the end, we will determine what is the most appropriate coarse-grained model of NFAs, taking into account a trade off between the accuracy and complexity of the model.

This paper is organized as follows: We start with a description of the methodology, followed by a discussion of the electronic

structure of isolated ITIC-4F molecule as a typical representative of the A–D–A class of molecules. Next, we investigate the stability of various coarse-grained bases with respect to different types of geometrical distortions and then analyze fluctuations of tight-binding (TB) elements. Finally, we study how errors in coarse-graining influence calculated charge transport properties.

## II. METHODOLOGY

Localized molecular orbitals (LMO) are obtained by orthogonal projection of canonical MOs onto the basis of the selected block of atoms. In fact, the choice of localization procedure is noncritical for the scope of this work. Nevertheless, a reference to the localization algorithm and code is given in supplementary material. The methodology has been thoroughly tested for organic,<sup>22</sup> metal-organic,<sup>25</sup> and inorganic<sup>26</sup> semiconductors. Multiple LMO models are employed, designated as  $N$ -LMO, where  $N$  represents the number of localized molecular orbitals utilized in the model.

One of the aims of this work is to grade various coarse-grained electronic bases. As a measure of basis quality, we take its ability to describe LUMO of a distorted molecule (all bases are naturally defined to give an exact LUMO for the undistorted geometry). Specifically, to evaluate the accuracy of a given basis of molecular orbitals  $\psi_1, \psi_2, \dots, \psi_n$  in approximating a target molecular orbital  $\psi'$ , we quantify the deviation using a norm of  $\Delta\psi' = \psi' - \sum_i c_i \psi_i$ . The key technical difficulty is how to define the coefficients  $c_i$  and the norm. Indeed,  $\psi_i$  and  $\psi'$  are provided in the same atomic orbital (AO) basis set but differently oriented and displaced due to different molecular geometry. Therefore, there is no obvious choice for the norm and for the procedure how coefficients  $c_i$  are determined. Since, in TB models, molecular deformations are encoded in the TB Hamiltonian parametrically, we do not transform the AO basis set (except for molecular block rotations) but consider only a vector space of coefficients itself. However, molecular deformations also change the AO overlap matrix ( $S$  for  $\psi_i$  and  $S'$  for  $\psi'$ ), and this change must be taken into account explicitly. The most straightforward solution is to orthogonalize the AO basis, and we consider this option with the symmetric orthogonalization  $\psi_i^\circ = \sqrt{S}\psi_i$ ,  $\psi'^\circ = \sqrt{S'}\psi'$ . Then, the natural choice for the norm is Euclidean. However, to keep the overall complexity at the level of matrix multiplication, the calculation of the square root of a matrix should be avoided. Although there is no obvious choice for the norm in this case, the generalized Euclidean norm seems to be reasonable: one with the undistorted overlap matrix  $S$ , which is the default method, and another one with the unit overlap. Since all the mentioned norms are quadratic, we define the *basis deficiency* as  $\|\Delta\psi'\|^2$  with three alternative interpretations of the norm symbol:  $\|\cdot\|_2$  for the Euclidean norm,  $\|\cdot\|_S$  for the generalized Euclidean norm with the overlap matrix of the undistorted molecule, and  $\|\cdot\|_0$  for the Euclidean norm in the orthogonalized basis. If the norm is the generalized Euclidean and  $\psi_i$  are orthonormal in this norm, then coefficients  $c_i = \psi_i^+ S \psi'$  minimize  $\|\Delta\psi'\|$  so that the basis set deficiency becomes  $\|\Delta\psi'\|^2 = \psi'^+ S \psi' - \sum_i |\psi_i^+ S \psi'|^2$ , where  $\psi^+$  means the Hermitian conjugate. In other cases, the minimization is more complicated, and the resulting expression for  $c_i$  is less meaningful. For this reason, we fix  $c_i = \psi_i^+ S \psi'$  for all considered norms. If  $\psi_i$  is a LMO, it is rotated together with its biorthogonal vector  $\psi_i^+ S$ . The

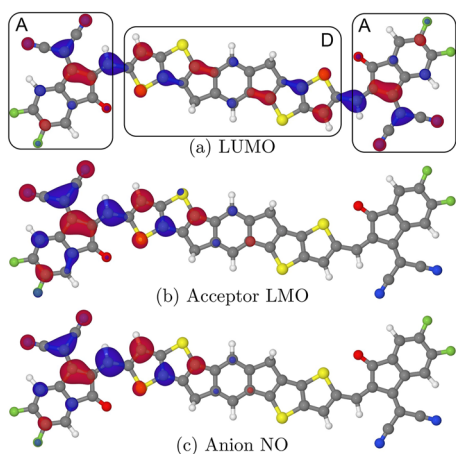


**FIG. 1.** Localization of electron wave-function on one of the two acceptor blocks: despite the LUMO of the undistorted ITIC-4F molecule being delocalized as in panel (a), the electron NO is typically localized on one of the two acceptor LMOs shown in panel (b), either due to molecular deformations or self-localization in a polarizable environment as illustrated for the anion NO in water-like polarizable continuum model in panel (c). See more examples in Fig. S16.

resulting set of LMOs becomes non-orthonormal but the LMO overlap is usually close to the unit matrix. Effects of local rotation of AOs due to geometric deformations are not considered.

The crystalline and partially ordered smectic morphologies are taken from classical MD simulations performed in Ref. 16. The MD supercell contains 2000 molecules, 500 of which are used in this analysis.

Technical details are given in Sec. S1 of supplementary material, including parameters of quantum chemistry calculations, comparison of different variations of the localization algorithms (Table S1), treatment of anharmonic vibrational modes (Table S2), and statistical analysis of simulated fluctuations (Table S3).

### III. RESULTS AND DISCUSSION

The electronic structure of ITIC-4F is typical for NFAs with the A–D–A structure:<sup>22</sup> the HOMO is localized on the donor block and is well separated from the next occupied MO, whereas the LUMO is quasi-degenerate [Fig. 1(a)] with only 0.2 eV separation between frontier MOs (Fig. S3). Further insight can be obtained by block-wise localization of several lowest unoccupied MOs as visualized in Fig. 2 (see also localization of the entire  $\pi$ -system in Fig. S5). It shows two weakly coupled lowest unoccupied LMOs localized on the two acceptors (see also Figs. S4 and S5 and Table S4). Consequently, the minimal coarse-grained model should include at least these two LMOs. In the 2-LMO model, the transfer integral is 120 meV, which is comparable with intermolecular acceptor-acceptor couplings in many NFAs, such as Y6, IDTBR, and ITIC.<sup>22</sup> The intramolecular electron transfer is transmitted through the donor block, but according to Fig. 2, multiple transfer channels exist with at least two lowest donor-block LMOs strongly coupled to the lowest acceptor-block LMOs. Therefore, the 6-LMO coarse-grained model (two LMOs per each block) should provide a more complete description of the low-energy electronic states, while being still separated from the LUMO of the  $\sigma$ -symmetry subsystem (see also Figs. S6 and S7). All LMOs in 2-, 4-, and 6-LMO models are visualized in Fig. S4, and the corresponding TB Hamiltonians are given in Table S4.

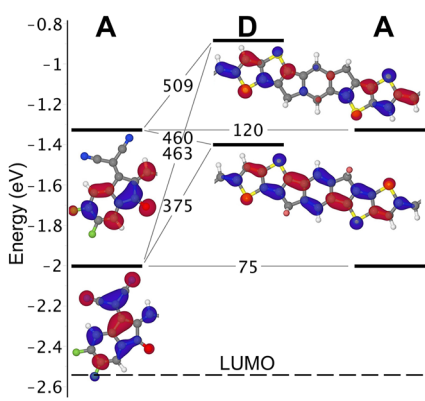


**FIG. 2.** 6-LMO coarse-grained model of ITIC-4F molecule. There are two LMOs per each block. The LMOs of the right-hand acceptor are not visualized since they mirror LMOs of the left-hand acceptor. Symmetry-unique inter-block electronic couplings (off-diagonal TB elements) are shown in meV. Here, the lowest LMO is more localized on the acceptor compared to the 2-LMO model shown in Fig. 1(b).

Inter-block connections are flexible but with a high rotation barrier of almost 0.5 eV, thus suppressing large amplitude librations. In the harmonic approximation, these librations are intermixed with other low-frequency vibrational modes (starting from 1 meV or  $5 \text{ cm}^{-1}$ ), corresponding to the in-plane and out-plane bending of the molecule. The  $180^\circ$ -flip of each dihedral costs only 50 meV, so conformers should be present in the amorphous phase.

Electron polaron is well localized on a single acceptor [Fig. 1(c)] in a highly polarizable environment with large energy gain relative to the symmetric charge distribution (270 meV in the water-like polarizable continuum model). In vacuum, the symmetric distribution is unstable but the relaxed anion natural orbital (NO) differs from the LUMO of the neutral molecule insignificantly (Fig. S16).

To study the influence of molecular fluctuations on the electronic structure, we use four statistical ensembles to mimic the effects of static and dynamic disorder, both classical and quantum in the latter case. The first two ensembles are obtained from a single snapshot of the room temperature classical MD of crystalline and amorphous (“smectic” phase) solid state ITIC-4F. Because the MD uses a classical force field whose accuracy is expected to be lower than DFT, we also generate harmonic vibrations in classical and quantum Boltzmann statistics (the other two ensembles). For this purpose, we use normal modes of the neutral molecule but with renormalized frequencies of several anharmonic modes, see Table S2 for details. Such renormalization does not treat mode mixing, resulting in an excess of higher-energy fluctuations (Fig. S1), as evidenced by the higher value of energy variation (Table S3). The quantum ensemble generates an excess of high-frequency modes via zero-energy vibrations: although these modes interact coherently with electronic degrees of freedom, the “decoupled” description of their influence on the electronic structure seems to be meaningful.

Statistical analysis of the electronic structure sampled in all four ensembles immediately shows that, in contrast to HOMO, the LUMO is unstable with respect to room-temperature fluctuations in the sense that, for the majority of distorted geometries, the LUMO differs substantially from the LUMO of the undistorted molecule (Figs. S8 and S10). Consequently, the combined effect of self-localization and distortion leads to complete localization of extra charge on a single acceptor even in crystal, see Fig. 3(a) [also Fig. 5(a), Fig. S8, Table S5, Fig. S16, and cf. HOMO in Fig. S17].

While the basis of two LUMOs of the unperturbed molecule is capable to describe the LUMO of the majority of molecular conformations in crystal, at least two LMOs are needed to describe the LUMO of molecular conformations in amorphous solid, see Fig. 3(b). In the latter case, the addition of a few other LMOs (6-LMO model) makes the LMO basis as accurate as the entire-band MO basis [Fig. 3(b)] but more robust with respect to large deformations (Fig. S11d).

Detailed analysis of extreme points in the sampled datasets shows three cases. If distortions are small, the LUMO is fully delocalized across the molecule, and any coarse-grained basis is accurate within a few percent, Fig. 4(a). In contrast, if distortions are substantial, the LUMO is localized on one of the acceptors, and the minimal coarse-grained basis should include at least two MOs or LMOs, whereas the use of the more accurate 6-LMO model reduces the basis deficiency to a few percent, Fig. 4(b). In the extreme cases of large-scale molecular deformations such as the  $90^\circ$ -rotation of

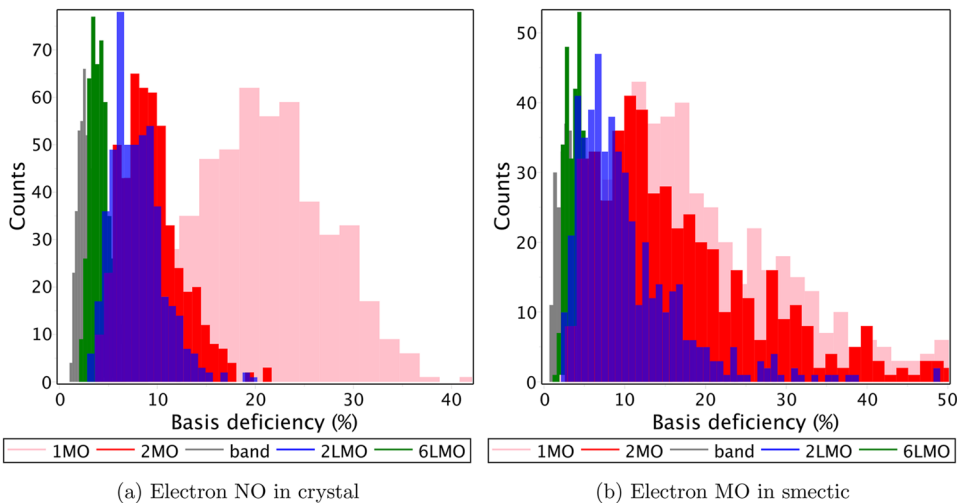


**FIG. 3.** Statistical analysis of the basis deficiency in a coarse-grained description of electron MO and NO (i.e., LUMO and anion NO). For the basis, we take two types of orbitals: canonical MOs and LMOs of the isolated fully relaxed molecule. The type and number of basis orbitals are indicated in the legend, whereas “band” means the orthogonalized basis of the entire unoccupied band. Panel (a) shows that the LUMO of the undistorted molecule fails to describe electron NO even in the crystal due to self-localization. Panel (b) shows that molecular deformations in the amorphous solid are so large that the rigid basis of MOs of the undistorted molecule gives a poor description even for electron MO (LUMO of the distorted molecule), whereas one LMO per acceptor block provides the minimum reasonable basis. See more histograms in Figs. S8–S10.

flexible dihedrals, the use of LMOs remains meaningful albeit with low accuracy, see Fig. S11d.

To make a more rigorous statement about electron localization, we analyze the distribution of coefficients of expansion of electron

MO and NO on the 2-LMO basis. We immediately see that the electron NO is localized on one of the acceptors in the majority of molecular conformations in both crystalline and amorphous solids, see Fig. 5. In contrast, LUMO shows no electron localization but only

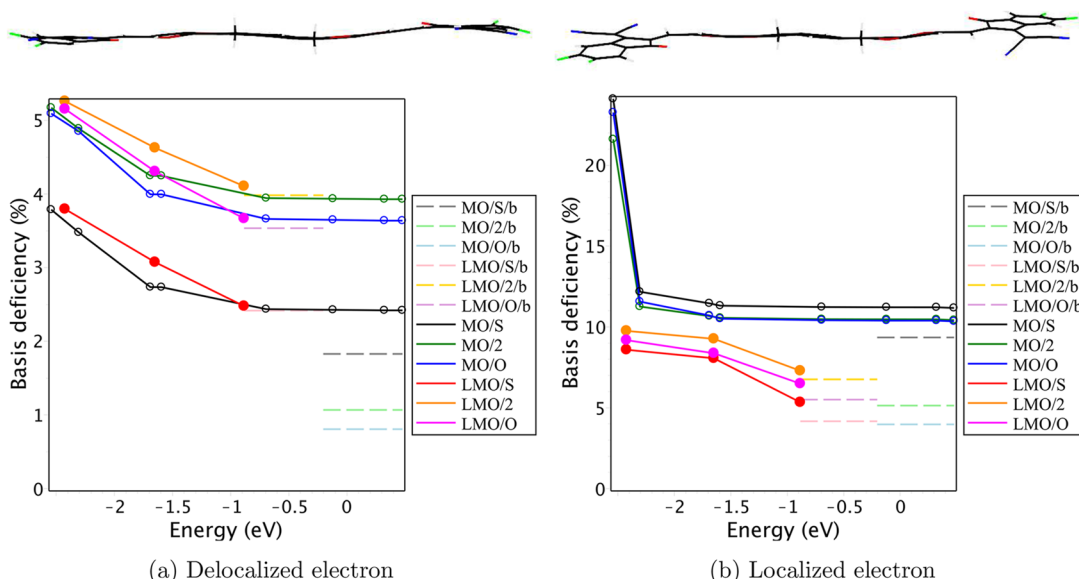


**FIG. 4.** Detailed analysis of two representative configurations: (a) LUMO is fully delocalized across the molecule and (b) LUMO is localized on one of the acceptors. Three vector norms are compared: Euclidean labeled as “/2,” generalized Euclidean “/S,” and Euclidean in the orthogonalized basis “/O.” Each dot counted from left to right corresponds to an increase of the basis by one MO or two LMOs whose highest energy is marked on the horizontal axis. Dashed lines show the band limit, also labeled as “/b” (in the case of LMOs it is the  $\pi$ -band limit). Obviously, any basis is good for small deformations captured in panel (a), whereas at least two MOs are required for case (b), and overall at a fixed size, LMO-basis is more robust. See more examples in Figs. S11 and S12.

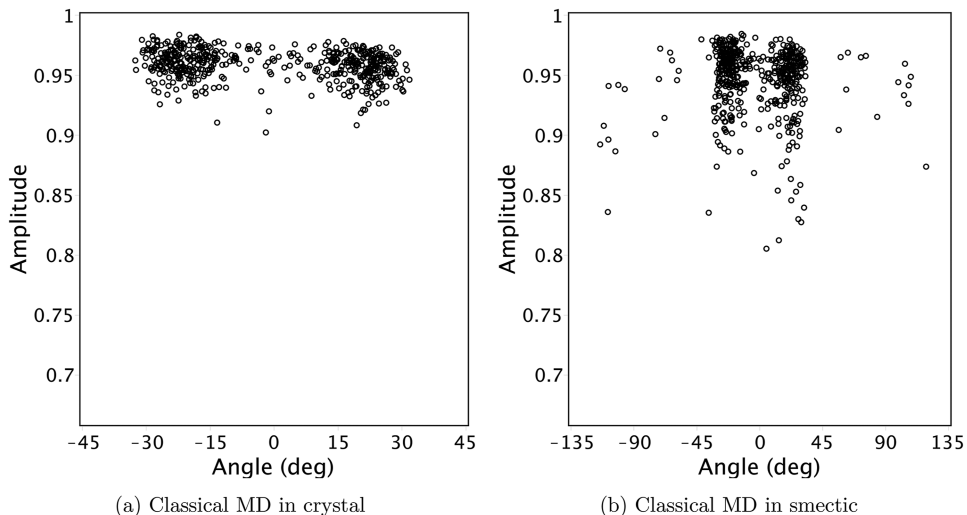


**FIG. 5.** (a) and (b) Coefficients of the expansion of electron NO of distorted molecules in two LMOs in polar representation rotated by 45°:  $c_1 = A \cos(\alpha + \pi/4)$  and  $c_2 = A \sin(\alpha + \pi/4)$ , where  $A$  is the amplitude and  $\alpha$  is the angle. In these notations,  $\alpha \approx \pm\pi/4$  corresponds to the wave-function localized on one of the two acceptors, whereas  $\alpha \approx 0$  corresponds to the delocalized wave-function; deviations of  $A$  from 1 are a measure of the basis deficiency. This figure clearly demonstrates the localization of the electron NO because points are segregated into two clusters corresponding to a localized wave-function. See also Figs. S13–S15, including Fig. S13a which exemplifies a delocalized wave-function.

a broad distribution of coefficients in the same range of angles (Fig. S13).

Having determined the optimal coarse-graining of the ITIC-4F molecule, we can analyze fluctuations of the TB Hamiltonian constructed in the 2-LMO and 6-LMO bases. In the first case, the intramolecular Hamiltonian is two-dimensional with three

parameters: average onsite energy  $(\epsilon_1 + \epsilon_2)/2$ , energy half-offset  $\epsilon = (\epsilon_2 - \epsilon_1)/2$ , and transfer integral  $t$ . Fluctuations of  $\epsilon$  and  $t$  in amorphous solids are plotted in Fig. 6(a), showing a single-centered distribution without a visual correlation between  $\epsilon$  and  $t$ . The standard deviations are 50 and 25 meV, respectively, which is much smaller than the absolute value of  $t$ , see Table S10. This means that

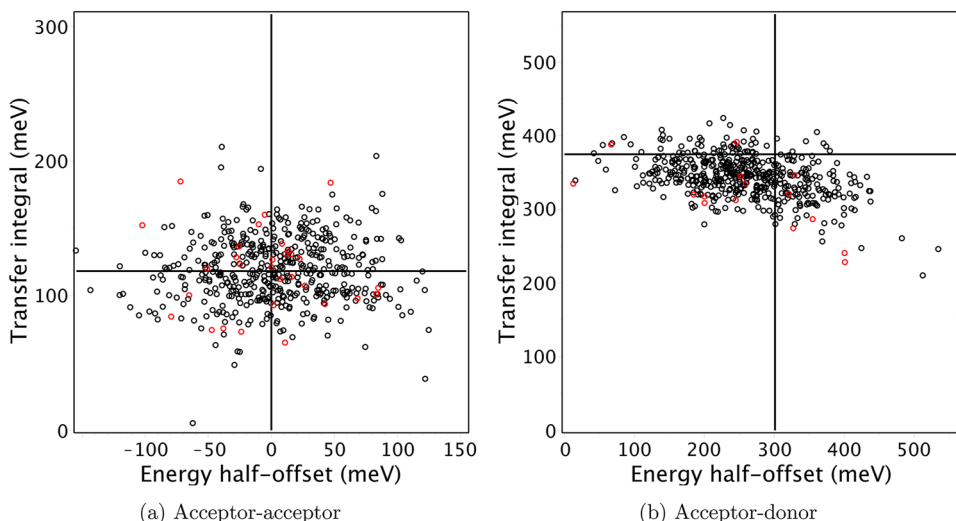


**FIG. 6.** Fluctuations of energy half-offset  $\epsilon$  and transfer integral  $t$  in amorphous solid (smectic). Scales of horizontal and vertical axes are made equal to emphasize that onsite energies undergo larger fluctuations. Red dots show negative values taken with opposite signs, which correspond to flipped acceptor blocks. The crossing gridlines mark values for undistorted geometry. Panel (a) shows the Hamiltonian elements of the minimum model of 2 LMOs, whereas, in panel (b), the 6-LMO model is used (2 per each block). See other TB elements in Figs. S18–S20.

the two acceptor blocks are always strongly coupled, and the main disorder effects are in onsite energy fluctuations. Interestingly, both the mean value and standard deviation of  $\epsilon$  and  $t$  are nearly the same for crystal, amorphous solid, and classical vibrations of the isolated molecule (Table S10), implying that the environmental effects have a minor influence on intramolecular energetics, despite having a large influence on type and amplitude of geometrical distortions. In contrast, quantum effects, such as zero-point vibrations, almost double the standard deviations (Fig. S18), thus emphasizing the importance of quantum treatment of high-frequency modes<sup>5</sup> (see the caption to Table S10). For the 6-LMO model, fluctuations of acceptor–donor energy offset show a bias toward lower values, see Fig. 6(b), thus explaining why this model provides a noticeably better description of LUMO under large distortions.

To understand how errors in the coarse-graining of individual molecules influence the accuracy of the calculation of electronic properties of a molecular solid, one has to distinguish two cases. If we calculate the electronic structure at fixed positions of atoms, then the only thing important is the deficiency of the coarse-grained basis. Therefore, for crystals, the basis of two LMOs or two MOs gives an accurate description of the bottom of the conduction band, whereas the use of a single MO per molecule misses the intermixing of LUMO and the next LUMO by intermolecular couplings. In contrast, if we calculate charge carrier transport in the hopping regime, we assume that each site orbital remains unchanged upon geometry fluctuations, consequently using MOs for electrons in NFAs is inappropriate at all.

To quantify the error, we consider three topologies of electronic connectivity commonly observed in crystals of A–D–A molecules:<sup>22,27</sup> one-dimensional slipstack (EH-IDTBR), two-dimensional brickwork (ITIC-4F, Fig. S21), and three-dimensional wiremesh (*o*-IDTBR, Fig. S22). We compare 1-site vs 2-site models in terms of two electronic structure parameters: tensor of inverse effective masses and tensor of squared hopping amplitudes. Accuracy in the evaluation of these quantities contributes to the accuracy of electronic transport modeling because the charge carrier mobility is proportional to these parameters in the two limiting cases: scattering of free charge carriers and hopping of localized ones, see Section S4 in Ref. 22. Results of the comparison depend on multiple parameters including crystal geometry and electronic couplings and are compiled in Table S11. The main conclusion is that under the most typical conditions when the intramolecular transfer integral is substantially larger than intermolecular ones, the mobility is underestimated by a factor of two. This can be explained by the reduction of intermolecular transfer integrals by this factor due to intramolecular delocalization of the wave-function assumed in the 1-site model. In the case of comparable intra- and intermolecular couplings (best performing NFAs), the error of the 1-site model is less systematic but anisotropic by a factor of 2–3, implying that the mobility tensor is substantially distorted upon merge of the acceptor sites. For example, in brickwork geometry, the ratio of mobilities parallel and perpendicular to the long axis of the molecule can be overestimated by a factor of 3. In practice, anisotropy can be directly compared to single-crystal mobility measurements to distinguish between 1-site and 2-site models. In addition, the electronic band structure transforms significantly upon change of transfer integrals: for example, in brickwork geometry, which has a honeycomb topology of electronic connectivity, the band structure consists of

two sub-bands connected via Dirac cone if and only if the transfer integrals satisfy the triangle inequality (see Fig. S23).

We have demonstrated that the accurate coarse-grained electronic model of a molecular solid should involve proper coarse-graining of intramolecular electronic degrees of freedom: long flexible  $\pi$ -conjugated molecules require at least one electronic site per each electronically active rigid block. A robust coarse-grained basis is provided by localized molecular orbitals, whereas canonical MOs are unstable with respect to fluctuations of intramolecular geometry. In the case of A–D–A type molecules used as acceptor material in solar cells, the electron is localized on one of the acceptor blocks in the majority of molecular conformations in both crystalline and amorphous solids, so that LUMO of the unperturbed molecule is not representative at all. The resulting error in the estimation of charge carrier mobility and its anisotropy can be as large as a factor of 2. Importantly, this is a purely electronic contribution to the error, substantially exceeding errors of state-of-the-art DFT calculations of the electronic structure of organic semiconductors.

## SUPPLEMENTARY MATERIAL

The supplementary material contains details of the computational methodology and additional figures and tables on the electronic structure of undistorted and distorted conjugated backbone, fluctuations of TB Hamiltonian elements, and calculations of charge transport parameters.

## ACKNOWLEDGMENTS

We thank Wenlan Liu, Mukunda Mandal, and Naomi Kinaret for the fruitful discussions. This work was performed, in part, at the Center for Integrated Nanotechnologies, an Office of Science User Facility operated for the U.S. Department of Energy (DOE) Office of Science by Los Alamos National Laboratory (Contract No. 89233218CNA000001) and Sandia National Laboratories (Contract No. DE-NA-0003525). D.A. acknowledges the KAUST PSE Division for hosting his sabbatical in the framework of the Division's Visiting Faculty program. D.A. acknowledges funding by the Deutsche Forschungsgemeinschaft (DFG, German Research Foundation) for financial support through the collaborative research centers TRR 146, SPP 2196, and Grant No. 460766640.

## AUTHOR DECLARATIONS

### Conflict of Interest

The authors have no conflicts to disclose.

### Author Contributions

**Andriy Zhugayevych:** Conceptualization (lead); Data curation (equal); Formal analysis (equal); Investigation (lead); Methodology (equal); Project administration (lead); Supervision (equal); Validation (equal); Visualization (equal); Writing – original draft (equal); Writing – review & editing (equal). **Kun-Han Lin:** Data curation (supporting); Formal analysis (supporting); Investigation

(supporting); Methodology (equal). **Denis Andrienko:** Conceptualization (equal); Data curation (equal); Formal analysis (equal); Funding acquisition (lead); Investigation (equal); Methodology (equal); Project administration (equal); Resources (lead); Software (lead); Supervision (equal); Validation (equal); Visualization (equal); Writing – original draft (equal); Writing – review & editing (equal).

## DATA AVAILABILITY

The data that support the findings of this study are available within the article and its supplementary material.

## REFERENCES

- <sup>1</sup>S. R. Forrest, *Organic Electronics: Foundations to Applications* (OUP, 2020).
- <sup>2</sup>P. Friederich, A. Fediai, S. Kaiser, M. Konrad, N. Jung, and W. Wenzel, “Toward design of novel materials for organic electronics,” *Adv. Mater.* **31**, 1808256 (2019).
- <sup>3</sup>S. Hutsch, M. Panhans, and F. Ortmann, “Charge carrier mobilities of organic semiconductors: *Ab initio* simulations with mode-specific treatment of molecular vibrations,” *npj Comput. Mater.* **8**, 228 (2022).
- <sup>4</sup>T. Nematiaran and A. Troisi, “Modeling charge transport in high-mobility molecular semiconductors: Balancing electronic structure and quantum dynamics methods with the help of experiments,” *J. Chem. Phys.* **152**, 190902 (2020).
- <sup>5</sup>Y. Jiang, H. Geng, W. Li, and Z. Shuai, “Understanding carrier transport in organic semiconductors: Computation of charge mobility considering quantum nuclear tunneling and delocalization effects,” *J. Chem. Theory Comput.* **15**, 1477 (2019).
- <sup>6</sup>S. Fratini, D. Mayou, and S. Ciuchi, “The transient localization scenario for charge transport in crystalline organic materials,” *Adv. Funct. Mater.* **26**, 2292 (2016).
- <sup>7</sup>J.-L. Brédas, D. Beljonne, V. Coropceanu, and J. Cornil, “Charge-transfer and energy-transfer processes in pi-conjugated oligomers and polymers: A molecular picture,” *Chem. Rev.* **104**, 4971 (2004).
- <sup>8</sup>S. Giannini and J. Blumberger, “Charge transport in organic semiconductors: The perspective from nonadiabatic molecular dynamics,” *Acc. Chem. Res.* **55**, 819 (2022).
- <sup>9</sup>L. Craciunescu, S. Wirsing, S. Hammer, K. Broch, A. Dreuw, F. Fantuzzi, V. Sivanesan, P. Tegeder, and B. Engels, “Accurate polarization-resolved absorption spectra of organic semiconductor thin films using first-principles quantum-chemical methods: Pentacene as a case study,” *J. Phys. Chem. Lett.* **13**, 3726 (2022).
- <sup>10</sup>S. G. Engelbrecht, M. Prinz, T. R. Arend, and R. Kersting, “Terahertz spectroscopy on hole transport in pentacene thin films,” *Appl. Phys. Lett.* **105**, 012101 (2014).
- <sup>11</sup>F. Brown-Altvater, G. Antonius, T. Rangel, M. Giantomassi, C. Draxl, X. Gonze, S. G. Louie, and J. B. Neaton, “Band gap renormalization, carrier mobilities, and the electron-phonon self-energy in crystalline naphthalene,” *Phys. Rev. B* **101**, 165102 (2020).
- <sup>12</sup>B. K. Chang, J.-J. Zhou, N.-E. Lee, and M. Bernardi, “Intermediate polaronic charge transport in organic crystals from a many-body first-principles approach,” *npj Comput. Mater.* **8**, 63 (2022).
- <sup>13</sup>H. Oberhofer, K. Reuter, and J. Blumberger, “Charge transport in molecular materials: An assessment of computational methods,” *Chem. Rev.* **117**, 10319 (2017).
- <sup>14</sup>J. Niklas, K. L. Mardis, and O. G. Poluektov, “Spin signature of the C<sub>60</sub> fullerene anion: A combined X- and D-band EPR and DFT study,” *J. Phys. Chem. Lett.* **9**, 3915 (2018).
- <sup>15</sup>T. J. Aldrich, M. Matta, W. Zhu, S. M. Swick, C. L. Stern, G. C. Schatz, A. Facchetti, F. S. Melkonyan, and T. J. Marks, “Fluorination effects on indacenodithienothiophene acceptor packing and electronic structure, end-group redistribution, and solar cell photovoltaic response,” *J. Am. Chem. Soc.* **141**, 3274 (2019).
- <sup>16</sup>F. H. Hasenburg, K.-H. Lin, B. van der Zee, P. W. M. Blom, D. Andrienko, and G.-J. A. H. Wetzelar, “Ambipolar charge transport in a non-fullerene acceptor,” *APL Mater.* **11**, 021105 (2023).
- <sup>17</sup>X. Wan, C. Li, M. Zhang, and Y. Chen, “Acceptor-donor-acceptor type molecules for high performance organic photovoltaics - chemistry and mechanism,” *Chem. Soc. Rev.* **49**, 2828 (2020).
- <sup>18</sup>C. Poelking, J. Benduhn, D. Spoltore, M. Schwarze, S. Roland, F. Piersimoni, D. Neher, K. Leo, K. Vandewal, and D. Andrienko, “Open-circuit voltage of organic solar cells: Interfacial roughness makes the difference,” *Commun. Phys.* **5**, 307 (2022).
- <sup>19</sup>A. Markina, K. H. Lin, W. Liu, C. Poelking, Y. Firdaus, D. R. Villalva, J. I. Khan, S. H. K. Paleti, G. T. Harrison, J. Gorenflo, W. Zhang, S. De Wolf, I. McCulloch, T. D. Anthopoulos, D. Baran, F. Laquai, and D. Andrienko, “Chemical design rules for non-fullerene acceptors in organic solar cells,” *Adv. Energy Mater.* **11**, 2102363 (2021).
- <sup>20</sup>M. Saladina, P. Simón Marqués, A. Markina, S. Karuthedath, C. Wöpke, C. Göhler, Y. Chen, M. Allain, P. Blanchard, C. Cabanatos, D. Andrienko, F. Laquai, J. Gorenflo, and C. Deibel, “Charge photogeneration in non-fullerene organic solar cells: Influence of excess energy and electrostatic interactions,” *Adv. Funct. Mater.* **31**, 2007479 (2020).
- <sup>21</sup>Y. Firdaus, V. M. Le Corre, S. Karuthedath, W. Liu, A. Markina, W. Huang, S. Chattopadhyay, M. M. Nahid, M. I. Nugraha, Y. Lin, A. Seitkhan, A. Basu, W. Zhang, I. McCulloch, H. Ade, J. Labram, F. Laquai, D. Andrienko, L. J. A. Koster, and T. D. Anthopoulos, “Long-range exciton diffusion in molecular non-fullerene acceptors,” *Nat. Commun.* **11**, 5220 (2020).
- <sup>22</sup>S. Halaby, M. W. Martynowycz, Z. Zhu, S. Tretiak, A. Zhugayevych, T. Gonen, and M. Seifrid, “Microcrystal electron diffraction for molecular design of functional non-fullerene acceptor structures,” *Chem. Mater.* **33**, 966 (2021).
- <sup>23</sup>J. F. Galindo, E. Atas, A. Altan, D. G. Kuroda, S. Fernandez-Alberti, S. Tretiak, A. E. Roitberg, and V. D. Kleiman, “Dynamics of energy transfer in a conjugated dendrimer driven by ultrafast localization of excitations,” *J. Am. Chem. Soc.* **137**, 11637 (2015).
- <sup>24</sup>B. Smith and A. V. Akimov, “Modeling nonadiabatic dynamics in condensed matter materials: Some recent advances and applications,” *J. Phys. Condens. Matter* **32**, 073001 (2020).
- <sup>25</sup>R. R. Kapaev, A. Zhugayevych, S. V. Ryazantsev, D. A. Aksyonov, D. Novichkov, P. I. Matveev, and K. J. Stevenson, “Charge storage mechanisms of a π-d conjugated polymer for advanced alkali-ion battery anodes,” *Chem. Sci.* **13**, 8161 (2022).
- <sup>26</sup>V. Vasilchenko, S. Levchenko, V. Perebeinos, and A. Zhugayevych, “Small polarons in two-dimensional pnictogens: A first-principles study,” *J. Phys. Chem. Lett.* **12**, 4674 (2021).
- <sup>27</sup>D. Li, X. Zhang, D. Liu, and T. Wang, “Aggregation of non-fullerene acceptors in organic solar cells,” *J. Mater. Chem. A* **8**, 15607 (2020).

# Supplementary Material for Electronic coarse-graining of long conjugated molecules: case study of non-fullerene acceptors

Andriy Zhugayevych, Kun-Han Lin, Denis Andrienko

*Max Planck Institute for Polymer Research, Ackermannweg 10, 55128 Mainz, Germany*

June 14, 2023

S1	Computational methodology and abbreviations . . . . .	S2
S2	Geometric definitions . . . . .	S6
S3	Electronic structure of the conjugated backbone . . . . .	S7
S4	Electronic structure of distorted conjugated backbone . . . . .	S12
S5	Fluctuations of tight-binding Hamiltonian . . . . .	S27
S6	Impact on charge transport parameters . . . . .	S31

## S1 Computational methodology and abbreviations

a3p	Ahrlrichs triple- $\zeta$ basis Def2-TZVP	MO	Molecular Orbital
AO	Atomic Orbital	NFA	Non-Fullerene Acceptor
BLA	Bond Length Alternation	NO	Natural Orbital
CPCM	Conduct. Polarizable Continuum Model	NTO	Natural Transition Orbital
DFT	Density Functional Theory	PES	Potential Energy Surface
HOMO	Highest Occupied Molecular Orbital	p2p	Pople double- $\zeta$ polarized basis 6-31G*
LMO	Localized Molecular Orbital	TB	Tight Binding
LUMO	Lowest Unoccupied Molecular Orbital	TDDFT	Time Dependent DFT
MD	Molecular Dynamics	ZPE	Zero-Point Energy

The computational protocol and link to the open-source code ‘LocalizeMO’ used for localization of molecular orbitals are given in Ref. [LMO].

Relaxed anions of a multimer (oligomer or cluster of molecules) are obtained by providing a starting geometry in which one monomer (rigid molecular block) is replaced by its anion geometry (the code is MolMod/exam\_Geometry.mw/Molecules: Substitute fragment [MolMod]). The charge localization is then characterized by the half-occupied NO which is naturally called *anion NO* (normally there is one and only one NO with occupation 1, and occupations of other NOs are close to 0 or 2).

For calculations of molecules and their multimers we use CAM-B3LYPp2p method as implemented in Gaussian 16 package [Gaussian]. The CAM-B3LYP functional is chosen according to its proven reliability for  $\pi$ -conjugated molecules as it has been benchmarked in our previous publications [Tukachev19, Zhugayevych18, Zhugayevych16]. The basis 6-31G\*, referred here as ‘p2p’, provides a reasonable trade off between accuracy and scalability.

All classical MD simulations are performed using GROMACS 2020.3 package [GROMACS].

In all figures of the current work, the wave-function isovalue is about 0.03. In case of comparison, all figures are plotted with the same isovalue.

Vibrations are considered within the following Hamiltonian:

$$H = \frac{1}{2} \sum_{\alpha} M_{\alpha} \dot{x}_{\alpha}^2 + \frac{1}{2} \sum_{\alpha\beta} U''_{\alpha\beta} x_{\alpha} x_{\beta}, \quad (\text{S1})$$

where  $x_{\alpha}$  are coordinates of atoms,  $\mathbf{M}$  is the mass matrix and  $\mathbf{U}''$  is the force constants matrix. Let  $\{\Lambda, \mathbf{T}\}$  are the eigenelements of the spectral problem  $\mathbf{U}''\mathbf{T} = \mathbf{MT}\Lambda$  with the normalization  $\mathbf{T}^{\top}\mathbf{MT} = \mathbf{1}$ . Then the transformation

$$x_{\alpha} = \sum_{\beta} T_{\alpha\beta} \sqrt{\frac{\hbar}{\omega_{\beta}}} \xi_{\beta} \equiv \sum_{\beta} X_{\alpha\beta} \xi_{\beta}, \quad \xi_{\beta} = \sqrt{\frac{\omega_{\beta}}{\hbar}} \sum_{\alpha} x_{\alpha} M_{\alpha} T_{\alpha\beta} \quad (\text{S2})$$

diagonalizes the vibrational Hamiltonian:

$$H = \frac{1}{2} \sum_{\alpha} \hbar \omega_{\alpha} (\pi_{\alpha}^2 + \xi_{\alpha}^2 \operatorname{sgn} \Lambda_{\alpha}), \quad (\text{S3})$$

here  $\omega_{\alpha} = \sqrt{|\Lambda_{\alpha}|}$ ,  $\pi_{\alpha} = \dot{x}_{\alpha}/\omega_{\alpha}$ , and both  $\xi$  and  $\pi$  are dimensionless. In the thermal equilibrium, for each vibrational mode

$$\langle \xi^2 \rangle = \frac{a^2}{2}, \quad \text{where} \quad a^{\text{quantum}} = \sqrt{\coth \frac{\hbar\omega}{2T}}, \quad a^{\text{classical}} = \sqrt{\frac{2T}{\hbar\omega}} \quad (\text{S4})$$

are quantum and classical amplitudes. In the classical case, the potential energy, its average, and fluctuations are given by

$$E(\xi) = \frac{\hbar\omega\xi^2}{2}, \quad \langle E \rangle = \frac{\hbar\omega a^2}{4} \equiv \frac{T}{2}, \quad \langle \Delta E^2 \rangle = \frac{T^2}{2}. \quad (\text{S5})$$

To generate thermal displacements, normal random numbers are multiplied by  $a_{\alpha}/\sqrt{2}$  to get  $\xi_{\alpha}$ , and then the distorted molecular geometry is obtained by Eq. (S2).

Table S1: Comparison of different variations of the used localization algorithms (first column) in terms of the resulting tight-binding Hamiltonian for occupied (h35) and unoccupied (e27)  $\pi$ -LMOs localized from the corresponding complete band of MOs. Here the second and third columns give  $\sqrt{\min(N, N')^{-1} \sum_{ii'} H_{ii'}^2}$  where the sum is over all matrix elements (in eV) between two molecular blocks indicated in the head row (1=ICOC-F2, 2=IDTT, 3=ICOC-F2), i.e. rescaled Frobenius norm of the corresponding block of the Hamiltonian. The rest of columns give  $H_{ij}$  in eV where  $i$  is indicated in the fourth column and  $j$  is indicated in the rest of columns. The default algorithm “inU” is marked by asterisk.

	h35	1-2	1-3	25	34	33	32	35	28	30	31	29	26	27
outV	0.490	0.004	-7.066	0.324	0.323	0.284	0.151	0.110	-0.062	0.035	-0.021	0.009	0.002	
inV	0.490	0.004	-7.066	0.324	0.323	0.284	0.151	0.110	-0.062	0.035	-0.021	0.009	0.002	
out	0.491	0.004	-7.071	0.328	0.323	0.287	0.152	0.113	-0.063	0.035	-0.021	0.010	0.002	
in	0.491	0.005	-7.071	0.328	0.323	0.287	0.152	0.113	-0.063	0.035	-0.021	0.010	0.002	
inU*	0.493	0.005	-7.083	0.339	0.321	0.292	0.156	0.121	-0.066	0.036	-0.022	0.011	0.002	
outU	0.493	0.005	-7.083	0.339	0.321	0.292	0.156	0.121	-0.066	0.036	-0.022	0.011	0.002	

	e27	1-2	1-3	1	10	12	9	13	14	15	16	11	17	21
in	0.656	0.017	-1.992	-0.397	-0.372	-0.333	-0.292	0.190	0.157	-0.073	-0.069	-0.024	0.015	
outU	0.654	0.019	-1.989	-0.398	-0.368	-0.331	-0.290	0.186	0.155	-0.071	-0.069	-0.023	0.017	
inV	0.659	0.019	-1.975	-0.395	-0.365	-0.324	-0.288	0.183	0.152	-0.069	-0.070	-0.022	0.017	
inU*	0.654	0.020	-1.989	-0.398	-0.368	-0.330	-0.290	0.186	0.155	-0.071	-0.069	-0.023	0.017	
outV	0.659	0.021	-1.975	-0.395	-0.365	-0.324	-0.288	0.183	0.153	-0.069	-0.070	-0.022	0.017	
out	0.656	0.023	-1.992	-0.400	-0.369	-0.330	-0.294	0.188	0.159	-0.072	-0.068	-0.024	0.019	

Table S2: Scaling coefficients for anharmonic vibrational modes. Here  $\hbar\omega'$  is the rescaled frequency, and “energy ratio” is the ratio between total DFT energy and harmonic vibrational energy with the scaled frequency at the dimensionless displacement  $\xi = \sqrt{2T/\hbar\omega'}$  corresponding to  $T = 300$  K (cf. Eq. (S4)). The deviation is kept within 10% for all modes, but for high-frequency modes the actual deviation is much smaller. The scaling coefficients are obtained iteratively (displace by  $\xi$ , calculate DFT energy, update  $\hbar\omega'$ ) until the energy ratio is close to 1 (the code is [MolMod/exam\\_gau.mw/Vibrations/Calculate anharmonic frequencies](#) [MolMod]).

mode#	$\hbar\omega$ (meV)	$\hbar\omega'$ (meV)	scaling coef.	energy ratio
1	0.7	4.2	6.21	1.01
2	1.0	6.1	5.94	1.01
3	1.9	6.1	3.26	1.02
4	1.9	2.2	1.13	1.04
5	2.1	6.8	3.25	1.02
6	3.3	6.0	1.78	0.94
7	4.1	4.1	1	1.05
8	5.4	7.9	1.47	0.97
9	5.6	8.0	1.42	0.92
10	5.9	8.1	1.37	0.93
11	6.2	7.4	1.19	0.98
12	7.8	7.8	1	1.09

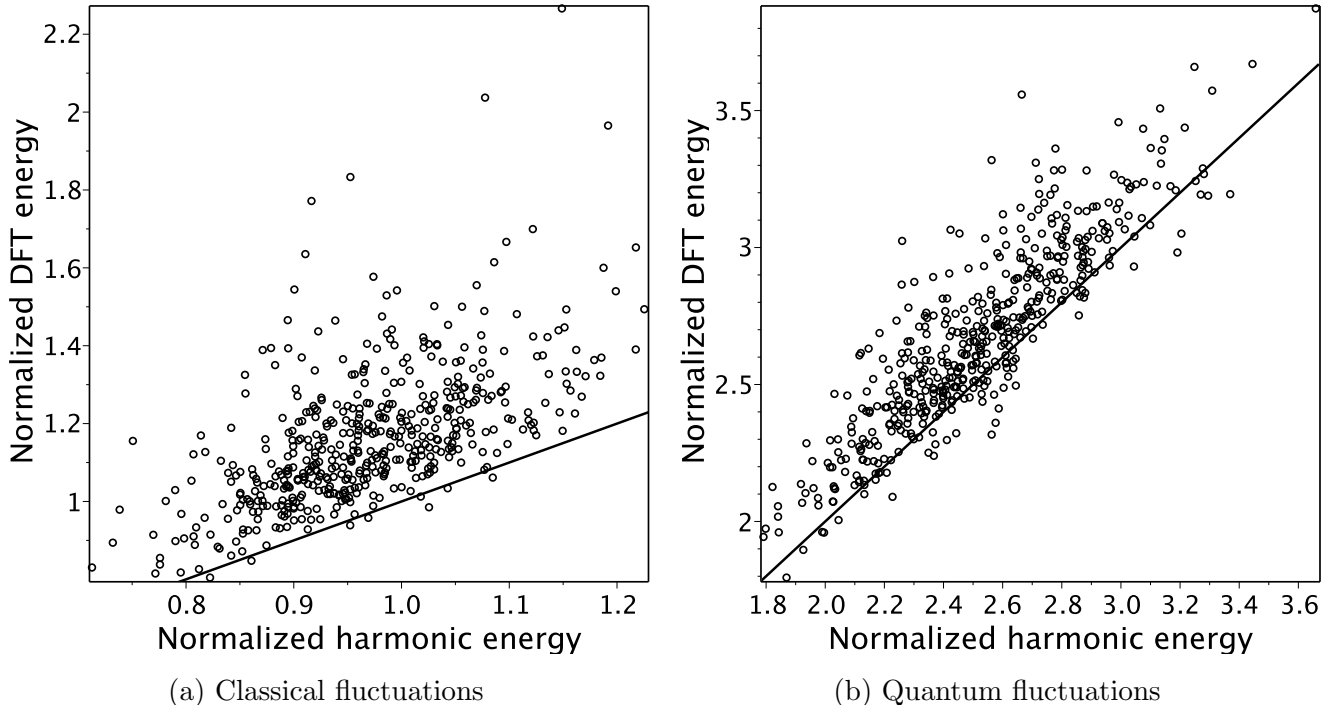


Figure S1: Correlation between total energy calculated in harmonic approximation and total DFT energy (relative to the ground state) for simulated disorder. The energy is normalized by  $NT/2$ , where  $N$  is the number of vibrational modes and  $T = 300$  K is the temperature. The line corresponds to 1:1 map. Because frequencies of anharmonic modes are rescaled individually, the deviation from that line is due to mode mixing.

Table S3: Effective vibrational temperatures for considered ensembles of molecular fluctuations defined to match exact bath temperature for the classical oscillator:  $T_{\text{eff1}} = 2\langle E \rangle / N$  and  $T_{\text{eff2}} = \sqrt{2\langle \Delta E^2 \rangle / N}$  where  $E$  is total DFT energy relative to the ground state (corresponds to the potential energy of the oscillator) and  $N$  is number of degrees of freedom (three per atom), see Eq. (S5).

dataset	$T_{\text{eff1}}(\text{K})$	$T_{\text{eff2}}(\text{K})$
Neutral molecule		
classical MD in crystal	384	418
classical MD in smectic	370	414
classical vibrations	339	546
quantum vibrations	781	1042
Anion		
classical MD in crystal	388	420
classical MD in smectic	376	425
classical vibrations	345	539
quantum vibrations	779	1038

## S2 Geometric definitions

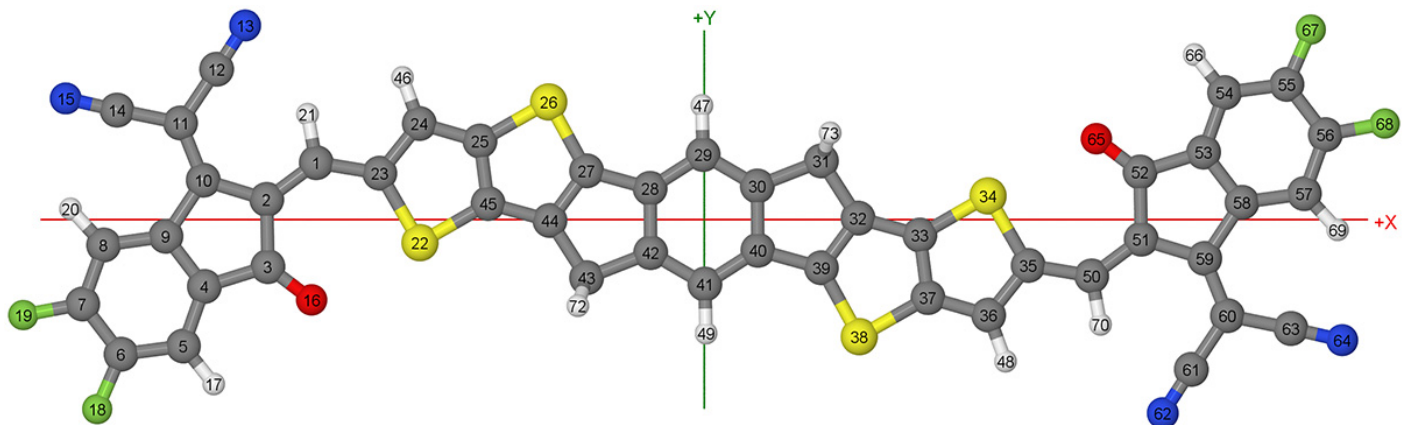


Figure S2: Orientation and atom indexing of the hydrogen-passivated  $\pi$ -conjugated backbone of ITIC-4F (**base** in filename notations). There are two flexible connections at bonds (1,23) and (35,50). The highest possible symmetry is  $2/m$ .

### S3 Electronic structure of the conjugated backbone

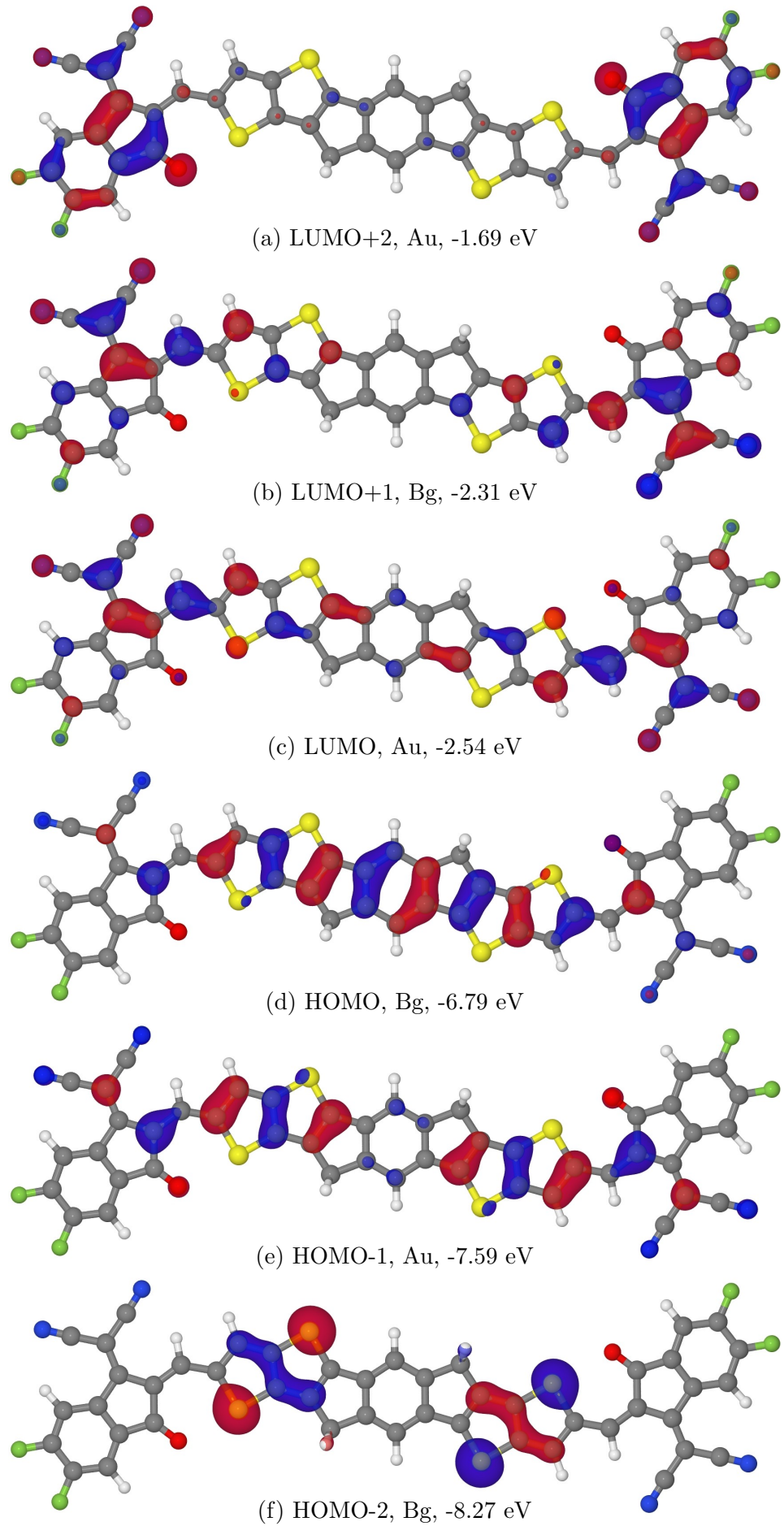


Figure S3: Frontier MOs of the conjugated backbone.

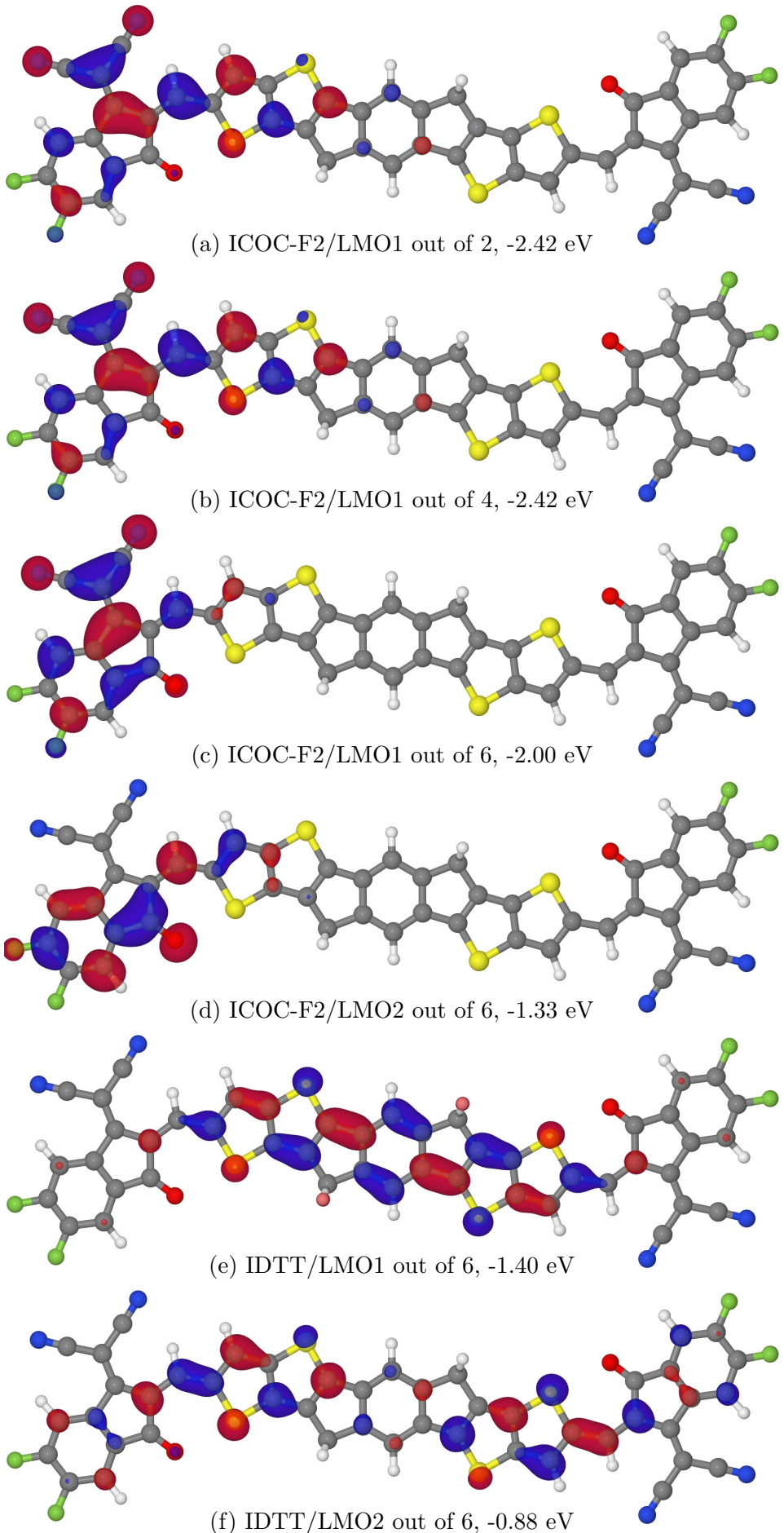


Figure S4: Lowest energy electron LMOs in three settings differing by number of MOs used for localization (that number is printed after “out of”).

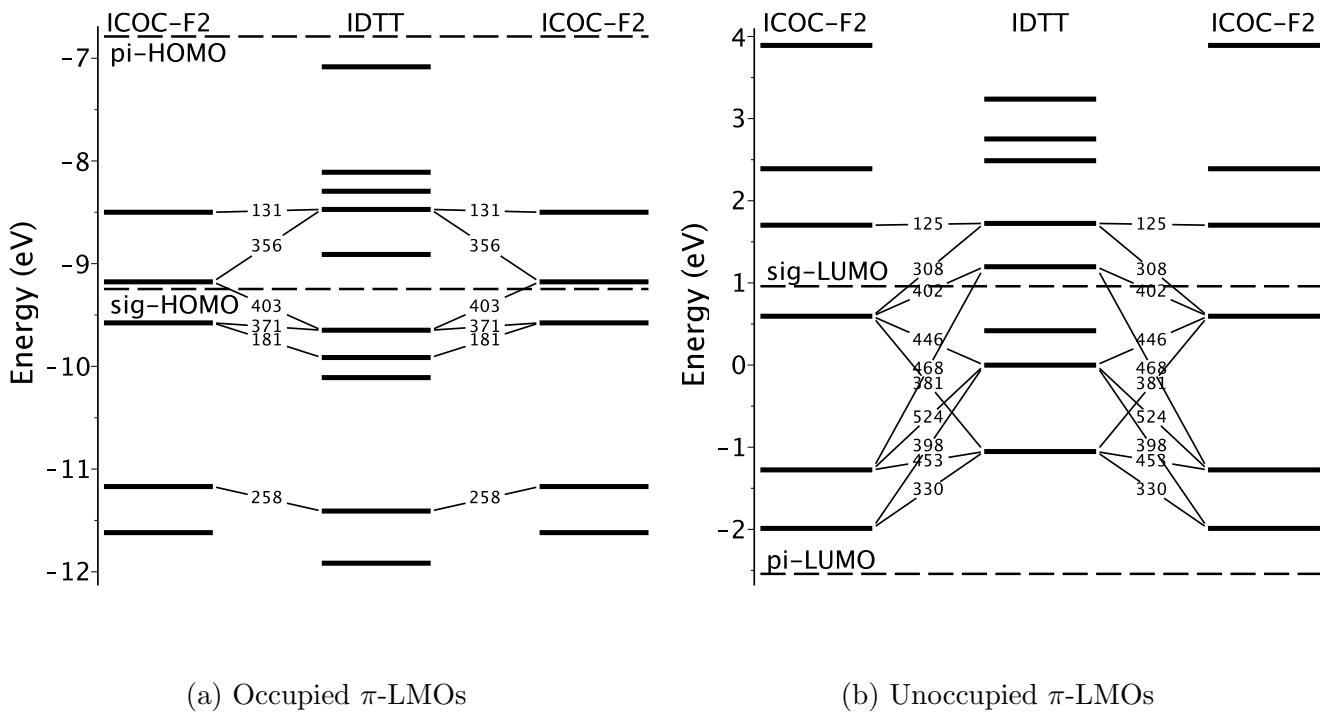


Figure S5: LMO diagram of the molecule. Only valence  $\pi$ -orbitals are considered (35 of them are occupied and 27 are vacant). Strongest ( $t^2/\Delta E > 100$  meV) electronic inter-block couplings are shown in meV. The analysis of couplings show that the lowest electron LMOs on the two acceptor blocks have negligible through-space coupling but are mainly coupled through the two lowest LMOs of the donor block with involvement of the second LMO on each acceptor block.

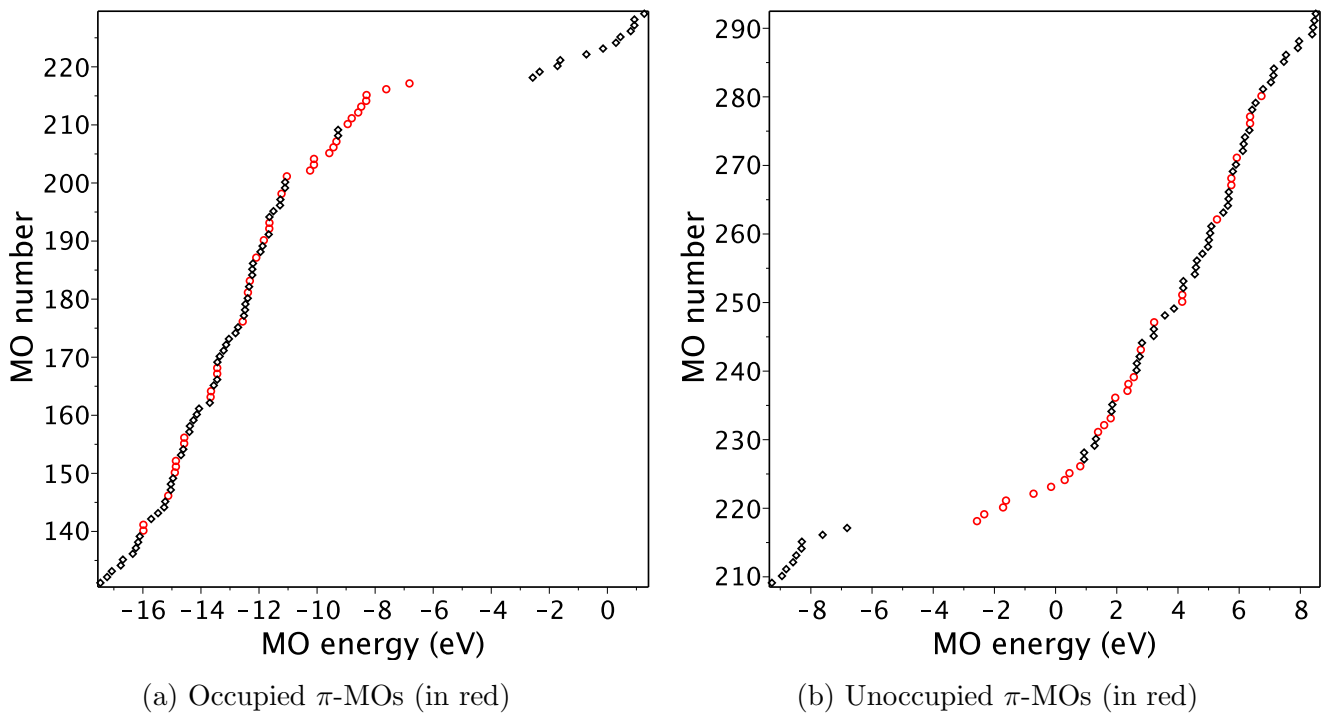


Figure S6: Energy distribution of  $\pi$ -MOs among other MOs.

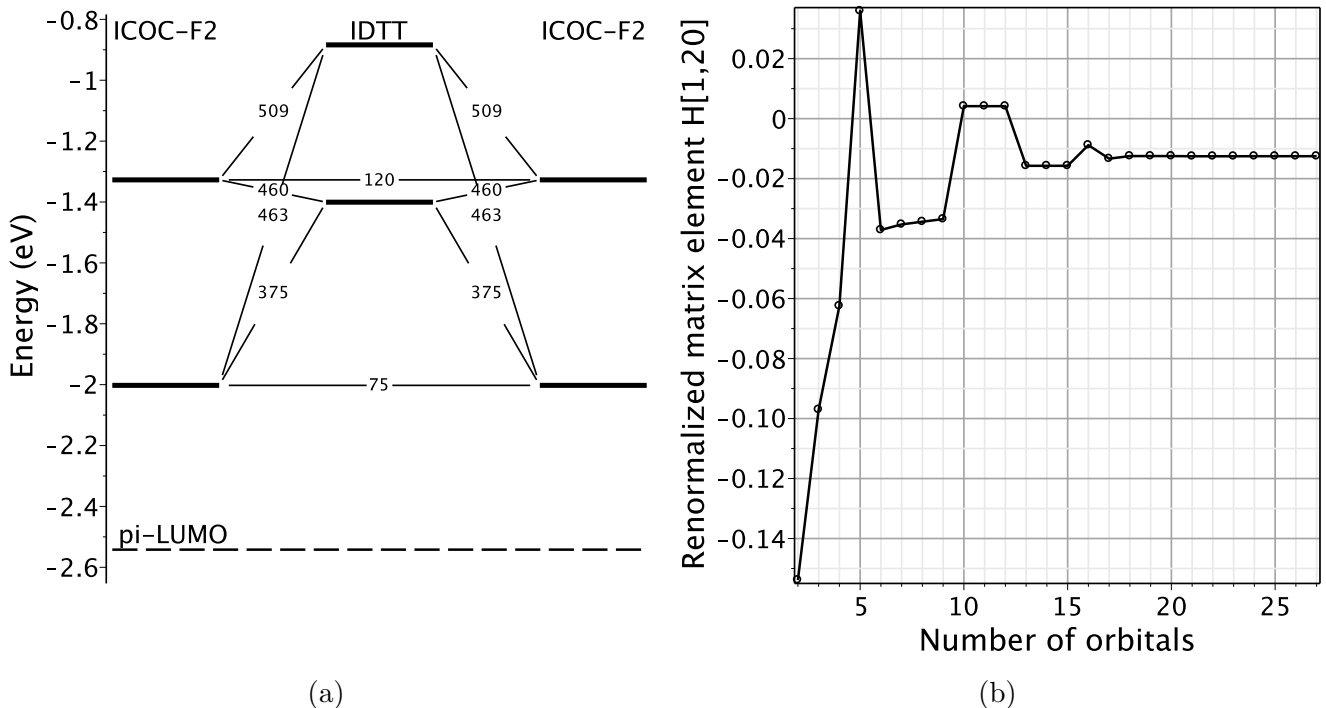


Figure S7: Analysis of the 6-LMO model. (a) LMO diagram. (b) Dependence of renormalized acceptor-acceptor transfer integral on number of orbitals included in sub-Hamiltonian. The renormalization is performed with the formula  $H'_{\text{sub}} = H_{\text{sub}} + V^+ (E_{\text{LUMO}} - H_{\text{rest}})^{-1} V$ , where the full Hamiltonian of  $\pi$ -electrons (27-LMO model) is partitioned according to  $H = \begin{pmatrix} H_{\text{sub}} & V^+ \\ V & H_{\text{rest}} \end{pmatrix}$ . Evidently, the renormalization strongly depends on number of orbitals until 6 of them, and then slowly approach full Hamiltonian limit, so that the 6-LMO model is the optimal model for detailed description of acceptor-acceptor transfer. Note that 5-LMO model is out of trend, that is why it is not used in this work.

Table S4: Tight-binding Hamiltonian (in eV) for LMOs shown in Fig. S4 and also for the entire  $\pi$ -band of unoccupied valence orbitals. The leading rows and columns are LMO energies used to index matrix elements of the Hamiltonian given in the rest of the table cells.

2 LMOs, lso1,lso2=[1] , [2]

H -----

.	-2.424
-2.424	-0.118

4 LMOs, lso1,lso2=[1..2] , [3..4]

-----

.	-2.416	-1.650
-2.416	-0.119	0.079
-1.650	0.079	-0.047

6 LMOs, lso1,lso2=[1..2] , [3..4,5..6]

-----

.	-1.401	-0.884	-2.002	-1.327
-2.002	-0.375	-0.463	-0.075	0.096
-1.327	0.460	0.509	0.096	-0.120

27 LMOs (entire pi-band), lso1,lso2=[1..8] , [9..19]

.	-1.053	-0.001	0.418	1.197	1.724	2.488	2.752	3.237	5.300	5.949	6.756
-1.989	-0.330	-0.398	-0.069	-0.368	-0.290	0.186	0.155	-0.071	-0.023	-0.013	.
-1.276	0.453	0.524	0.083	0.468	0.367	-0.275	-0.261	0.148	0.074	0.060	-0.021
0.594	-0.381	-0.446	-0.076	-0.402	-0.308	0.201	0.174	-0.089	-0.039	-0.028	0.006
1.702	-0.179	-0.202	-0.034	-0.171	-0.125	0.078	0.069	-0.038	-0.021	-0.017	0.005
2.390	-0.087	-0.105	-0.018	-0.097	-0.074	0.047	0.040	-0.019	-0.007	-0.005	.
3.891	-0.424	-0.499	-0.090	-0.443	-0.325	0.171	0.127	-0.053	-0.019	-0.010	-0.004
5.732	-0.200	-0.235	-0.042	-0.207	-0.150	0.077	0.056	-0.023	-0.009	-0.006	-0.001
6.379	-0.096	-0.106	-0.020	-0.081	-0.050	0.009	.	0.003	-0.001	.	-0.002

... continued, lso1,lso2=[1..8] , [20..27]

.	-1.989	-1.276	0.594	1.702	2.390	3.891	5.732	6.379
-1.989	-0.013	0.017	0.011	0.005	0.002	0.012	0.005	0.003
-1.276	0.017	-0.022	-0.014	-0.007	-0.003	-0.014	-0.007	-0.003
0.594	-0.011	0.014	0.009	0.004	0.002	0.008	0.004	0.002
1.702	-0.005	0.007	0.004	0.002	0.001	0.003	0.002	0.001
2.390	-0.002	0.003	0.002	0.001	.	0.001	0.001	.
3.891	-0.012	0.014	0.008	0.003	0.001	0.006	0.003	0.001
5.732	-0.005	0.007	0.004	0.002	0.001	0.003	0.001	0.001
6.379	-0.003	0.003	0.002	0.001	.	0.001	0.001	.

## S4 Electronic structure of distorted conjugated backbone

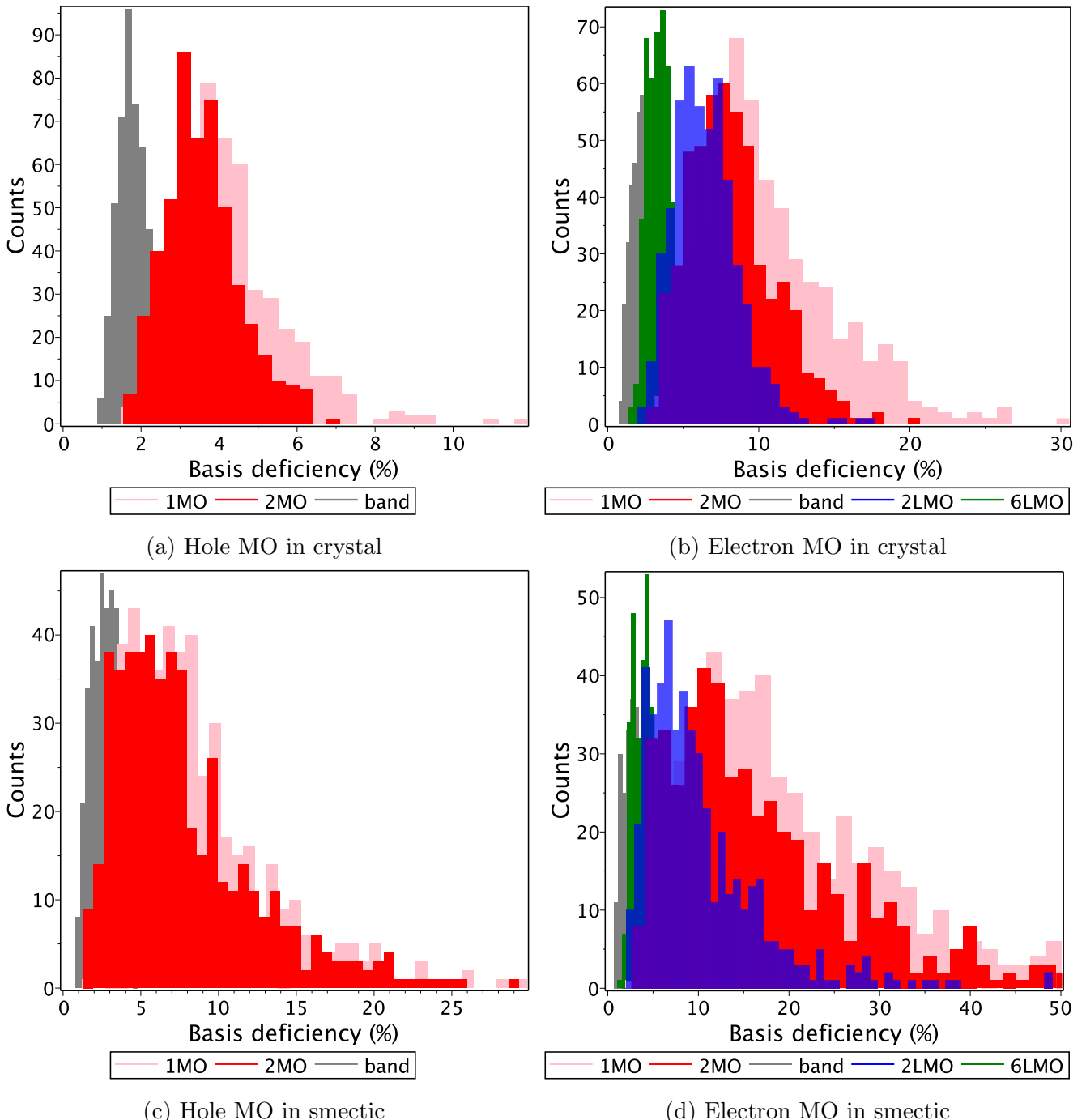
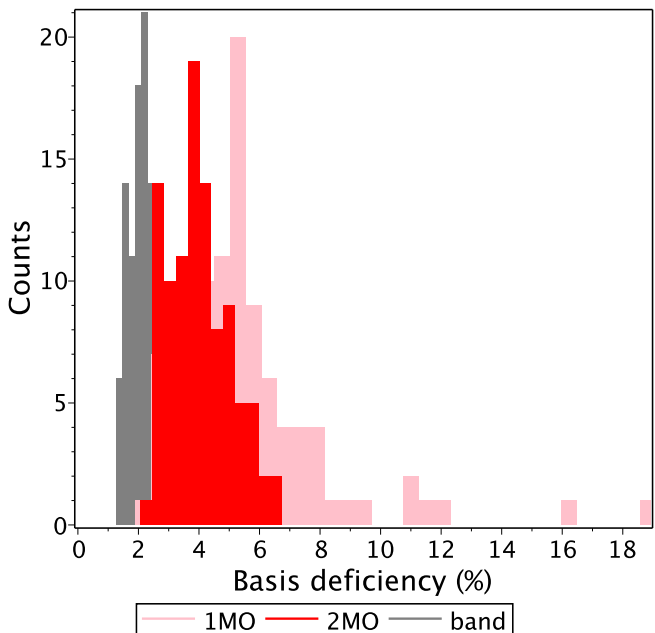
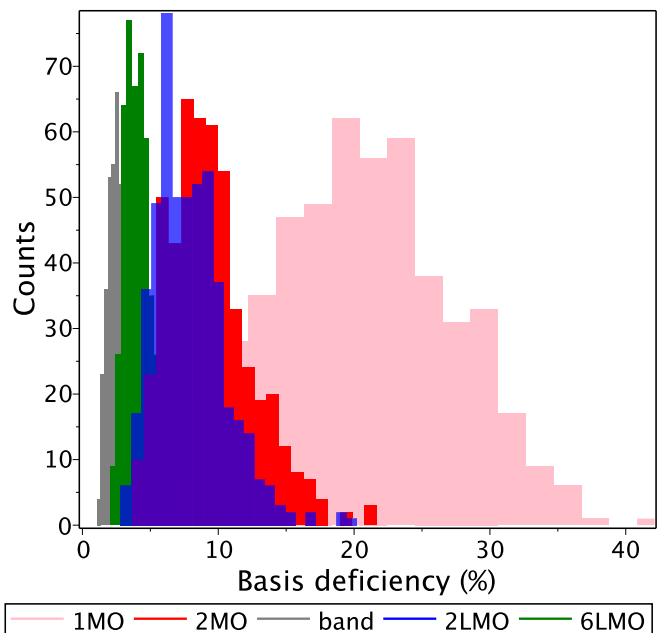


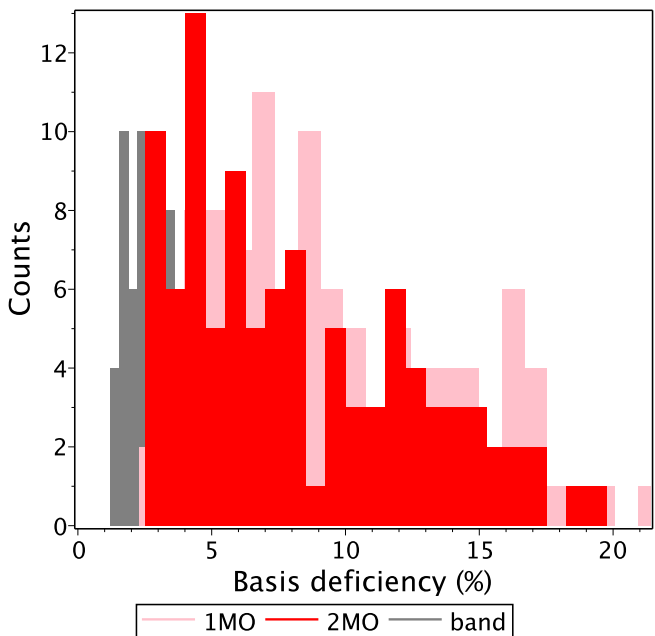
Figure S8: Statistical analysis of the basis deficiency in a coarse-grained description of HOMO/LUMO of distorted conjugated backbone using 500 conformations. For the basis we take two types of orbitals: canonical MOs (Fig. S3) and LMOs (Fig. S4) of the isolated fully relaxed backbone (reference geometry). The deficiency is calculated in the generalized Euclidean norm with the undistorted overlap matrix. The type and number of the basis orbitals is indicated in the legend, whereas “band” means sum over entire occupied or unoccupied band in the orthogonalized basis. Distorted configurations are taken from MD and superimposed onto the reference geometry.



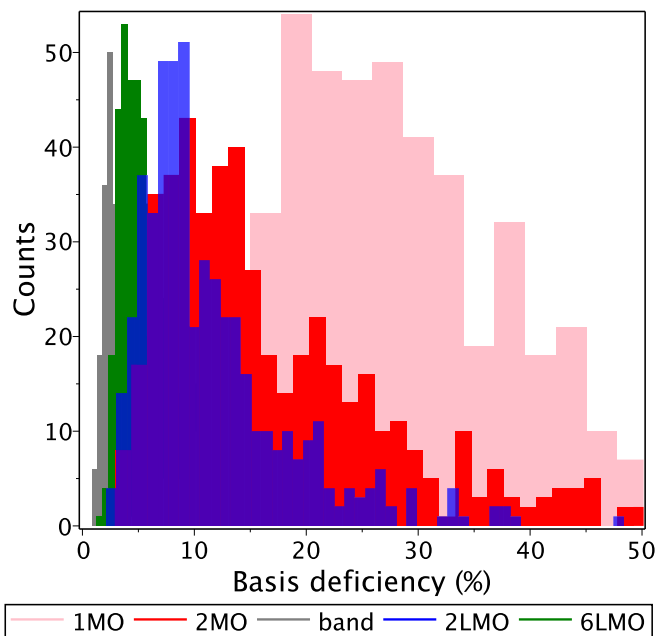
(a) Hole NO in crystal (100 conformations)



(b) Electron NO in crystal

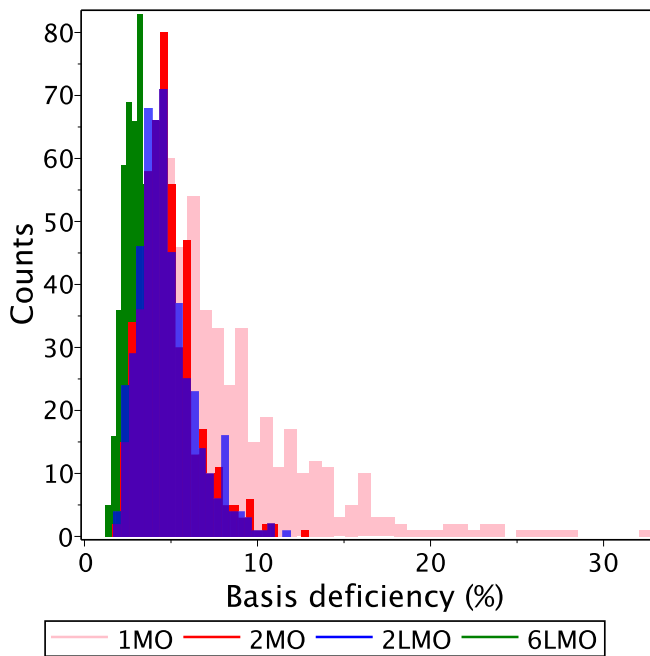


(c) Hole NO in smectic (100 conformations)

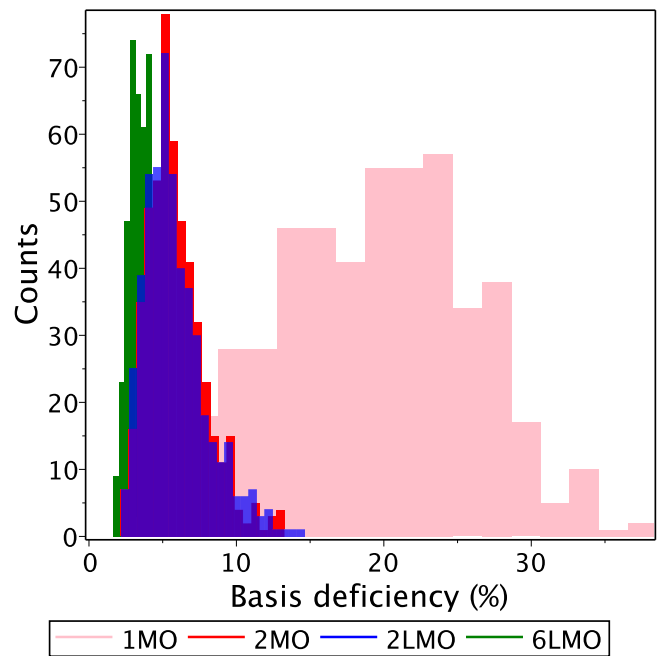


(d) Electron NO in smectic

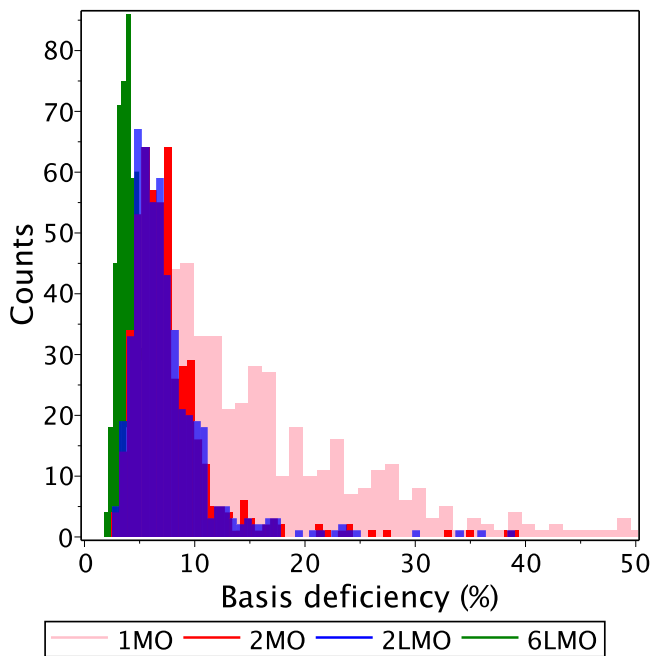
Figure S9: The same as Fig. S8 but with NO instead of MO.



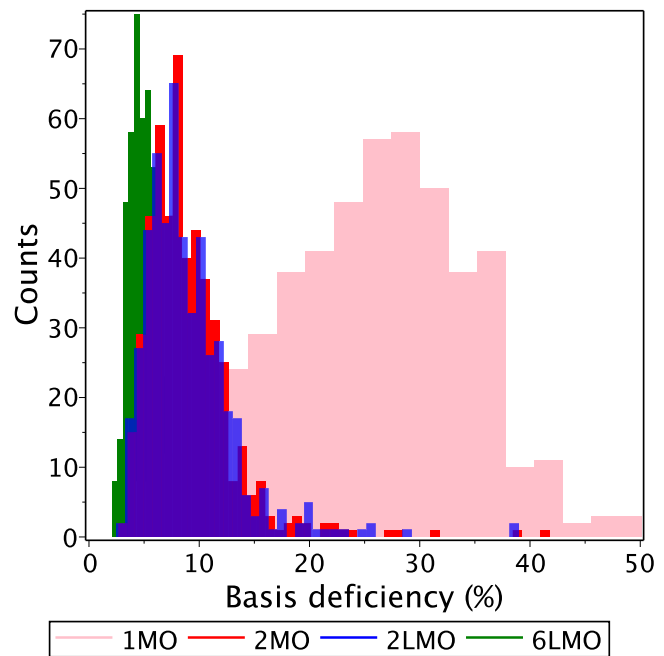
(a) Electron MO in classical fluctuations



(b) Electron NO in classical fluctuations



(c) Electron MO in quantum fluctuations



(d) Electron NO in quantum fluctuations

Figure S10: The same as Figs. S8 and S9 but with fluctuations generated by classical and quantum statistics of vibrations at 300 K.

Table S5: Statistical analysis of the basis deficiency using 500 conformations. See explanations in the caption of Fig. S8. All numbers are basis deficiencies in percents.

	1MO	2MO	band	2LMO	4LMO	6LMO	27LMO
LUMO in crystal							
Mean	9.0	6.1	1.4	5.0	4.4	2.7	2.4
Quantile-50	7.9	5.8	1.3	4.8	4.2	2.6	2.3
Quantile-75	10.7	7.2	1.7	5.9	5.2	3.3	3.0
Quantile-90	14.5	8.7	2.1	7.1	6.4	4.0	3.6
Anion NO in crystal							
Mean	20.6	9.4	6.3	7.9	6.7	4.3	3.9
Quantile-50	20.4	9.0	5.8	7.5	6.5	4.1	3.7
Quantile-75	25.2	11.0	7.7	9.4	8.0	4.9	4.5
Quantile-90	29.4	13.8	9.7	11.3	9.5	6.0	5.4
LUMO in smectic							
Mean	17.4	14.1	3.3	7.7	7.2	4.3	3.0
Quantile-50	14.6	10.9	2.4	6.4	6.0	3.7	2.7
Quantile-75	22.3	17.6	4.1	9.5	9.1	5.4	3.7
Quantile-90	31.3	26.6	6.4	13.6	13.1	7.6	5.2
Anion NO in smectic							
Mean	30.8	19.6	15.4	11.6	10.7	7.0	4.7
Quantile-50	27.3	14.5	11.0	9.2	8.3	5.6	4.1
Quantile-75	37.5	24.4	19.7	14.1	13.4	8.5	5.8
Quantile-90	48.8	37.9	32.5	20.8	20.3	12.7	7.7
Holes in crystal							
Mean	4.3	3.6	0.5				
Quantile-50	4.0	3.5	0.5				
Quantile-75	4.9	4.1	0.6				
Quantile-90	6.2	4.9	0.7				
Cation NO in crystal (100 conformations)							
Mean	5.6	4.0	1.0				
Quantile-50	5.2	3.9	0.9				
Quantile-75	6.2	4.7	1.1				
Quantile-90	8.0	5.5	1.2				
Holes in smectic							
Mean	8.4	7.8	1.1				
Quantile-50	7.4	6.7	0.9				
Quantile-75	10.5	9.8	1.3				
Quantile-90	15.0	14.1	2.1				
Cation NO in smectic (100 conformations)							
Mean	9.6	8.3	1.7				
Quantile-50	8.5	7.5	1.5				
Quantile-75	12.9	11.8	2.2				
Quantile-90	16.4	14.7	2.7				

Table S6: The same as Table S5 but with fluctuations generated by classical and quantum statistics of vibrations at 300 K..

	1MO	2MO	band	2LMO	4LMO	6LMO	27LMO
LUMO in classical fluctuations							
Mean	8.3	4.8	3.2	4.7	4.0	3.1	3.1
Quantile-50	7.1	4.5	3.1	4.4	3.8	3.0	3.0
Quantile-75	10.1	5.7	3.7	5.4	4.7	3.5	3.6
Quantile-90	14.0	7.0	4.6	6.9	5.6	4.3	4.2
Anion NO in classical fluctuations							
Mean	19.2	5.9	3.7	5.9	4.9	3.9	3.7
Quantile-50	19.8	5.6	3.6	5.4	4.6	3.7	3.5
Quantile-75	24.2	7.0	4.3	6.9	5.7	4.5	4.3
Quantile-90	27.9	8.5	5.4	9.0	6.9	5.4	5.2
HOMO in classical fluctuations							
Mean	3.8	3.1	0.5				
Quantile-50	3.5	3.0	0.5				
Quantile-75	4.4	3.6	0.6				
Quantile-90	5.5	4.2	0.7				
LUMO in quantum fluctuations							
Mean	15.4	7.7	3.9	7.5	5.2	4.1	3.8
Quantile-50	12.4	6.8	3.7	6.6	4.9	4.0	3.7
Quantile-75	19.7	8.7	4.5	8.4	5.9	4.7	4.3
Quantile-90	28.3	11.0	5.4	10.9	7.3	5.4	5.2
Anion NO in quantum fluctuations							
Mean	25.6	9.1	4.7	9.0	6.5	5.2	4.8
Quantile-50	25.9	8.3	4.5	8.1	6.2	4.9	4.6
Quantile-75	31.9	10.7	5.5	10.6	7.6	6.0	5.5
Quantile-90	36.3	13.1	6.7	13.3	9.2	7.2	6.7
HOMO in quantum fluctuations							
Mean	6.9	4.8	0.8				
Quantile-50	6.0	4.6	0.7				
Quantile-75	8.1	5.5	0.9				
Quantile-90	11.3	6.5	1.1				

Table S7: Statistical analysis of the basis deficiency using 500 conformations: comparison of three different algorithms. All numbers are basis deficiencies in percents.

	1MO	2MO	band	2LMO	4LMO	6LMO	27LMO
LUMO in crystal: generalized Euclidean norm							
Mean	10.9	8.2	6.1	6.5	6.0	3.6	3.4
Quantile-50	9.9	7.9	5.8	6.3	5.8	3.5	3.3
Quantile-75	13.4	9.8	7.5	7.8	7.2	4.1	4.0
Quantile-90	17.3	12.1	9.3	9.0	8.5	5.0	4.6
LUMO in crystal: Euclidean norm							
Mean	11.7	9.4	3.5	8.7	8.2	6.9	7.0
Quantile-50	11.1	9.1	3.3	8.5	8.0	6.6	6.7
Quantile-75	13.6	11.0	4.2	10.2	9.7	8.1	8.2
Quantile-90	16.5	12.7	5.2	11.8	11.3	9.3	9.5
LUMO in crystal: orthogonalized basis							
Mean	10.6	7.8	2.5	6.7	6.1	4.5	
Quantile-50	9.5	7.5	2.3	6.6	6.0	4.4	
Quantile-75	12.3	9.0	3.0	7.7	7.1	5.2	
Quantile-90	16.1	10.7	3.8	9.0	8.3	5.9	
LUMO in smectic: generalized Euclidean norm							
Mean	22.4	19.2	15.9	10.3	9.9	6.1	4.3
Quantile-50	17.9	14.6	11.9	8.4	8.4	5.1	3.8
Quantile-75	28.3	23.9	20.0	12.9	12.5	7.6	5.2
Quantile-90	40.6	36.8	31.5	18.0	17.5	10.8	6.9
LUMO in smectic: Euclidean norm							
Mean	17.4	14.7	8.5	10.0	9.6	7.6	7.3
Quantile-50	14.7	12.1	6.5	8.7	8.3	6.8	6.6
Quantile-75	21.7	17.9	10.7	12.1	12.0	9.4	8.8
Quantile-90	28.5	25.1	16.5	16.5	16.6	12.5	11.5
LUMO in smectic: orthogonalized basis							
Mean	19.1	15.9	6.2	9.5	9.1	6.2	
Quantile-50	16.2	12.9	4.6	8.2	7.8	5.5	
Quantile-75	23.9	19.4	7.8	11.4	10.9	7.4	
Quantile-90	33.0	27.9	11.9	15.7	15.3	9.6	

Table S8: Continuation of Table S7.

	1MO	2MO	band
HOMO in crystal: generalized Euclidean norm			
Mean	4.3	3.6	0.5
Quantile-50	4.0	3.5	0.5
Quantile-75	4.9	4.1	0.6
Quantile-90	6.2	4.9	0.7
HOMO in crystal: Euclidean norm			
Mean	4.3	3.8	2.8
Quantile-50	4.1	3.7	2.6
Quantile-75	4.9	4.4	3.2
Quantile-90	5.7	5.1	3.9
HOMO in crystal: orthogonalized basis			
Mean	4.1	3.5	1.8
Quantile-50	3.9	3.4	1.8
Quantile-75	4.7	4.0	2.1
Quantile-90	5.7	4.7	2.4
HOMO in smectic: generalized Euclidean norm			
Mean	8.4	7.8	1.1
Quantile-50	7.4	6.7	0.9
Quantile-75	10.5	9.8	1.3
Quantile-90	15.0	14.1	2.1
HOMO in smectic: Euclidean norm			
Mean	6.6	6.2	4.6
Quantile-50	6.0	5.4	4.1
Quantile-75	8.2	7.7	5.9
Quantile-90	10.9	10.5	7.9
HOMO in smectic: orthogonalized basis			
Mean	7.2	6.6	3.5
Quantile-50	6.5	5.8	3.1
Quantile-75	8.9	8.3	4.3
Quantile-90	12.1	11.4	6.1

Table S9: Table S5 with orthogonalized basis (see also Table S7 for explanations).

	1MO	2MO	band	2LMO	4LMO	6LMO
LUMO in crystal						
Mean	10.6	7.8	2.5	6.7	6.1	4.5
Quantile-50	9.5	7.5	2.3	6.6	6.0	4.4
Quantile-75	12.3	9.0	3.0	7.7	7.1	5.2
Quantile-90	16.1	10.7	3.8	9.0	8.3	5.9
Anion NO in crystal						
Mean	20.3	9.0	2.9	8.1	6.8	5.0
Quantile-50	20.4	8.7	2.7	7.8	6.5	4.8
Quantile-75	24.7	10.6	3.5	9.6	7.8	5.9
Quantile-90	28.8	12.6	4.4	11.5	9.5	6.9
LUMO in smectic						
Mean	19.1	15.9	6.2	9.5	9.1	6.2
Quantile-50	16.2	12.9	4.6	8.2	7.8	5.5
Quantile-75	23.9	19.4	7.8	11.4	10.9	7.4
Quantile-90	33.0	27.9	11.9	15.7	15.3	9.6
Anion NO in smectic						
Mean	27.7	16.5	6.4	10.8	9.7	6.8
Quantile-50	26.0	13.3	4.7	9.5	8.2	6.1
Quantile-75	33.6	19.9	7.9	12.9	11.5	8.0
Quantile-90	41.7	29.5	13.0	18.2	17.3	11.3
Holes in crystal						
Mean	4.1	3.5	1.8			
Quantile-50	3.9	3.4	1.8			
Quantile-75	4.7	4.0	2.1			
Quantile-90	5.7	4.7	2.4			
Cation NO in crystal (100 conformations)						
Mean	5.5	3.9	2.1			
Quantile-50	5.0	3.9	2.1			
Quantile-75	6.3	4.6	2.4			
Quantile-90	7.8	5.2	2.7			
Holes in smectic						
Mean	7.2	6.6	3.5			
Quantile-50	6.5	5.8	3.1			
Quantile-75	8.9	8.3	4.3			
Quantile-90	12.1	11.4	6.1			
Cation NO in smectic (100 conformations)						
Mean	8.4	7.2	3.8			
Quantile-50	7.9	6.6	3.4			
Quantile-75	11.1	10.2	5.1			
Quantile-90	13.6	12.4	6.3			

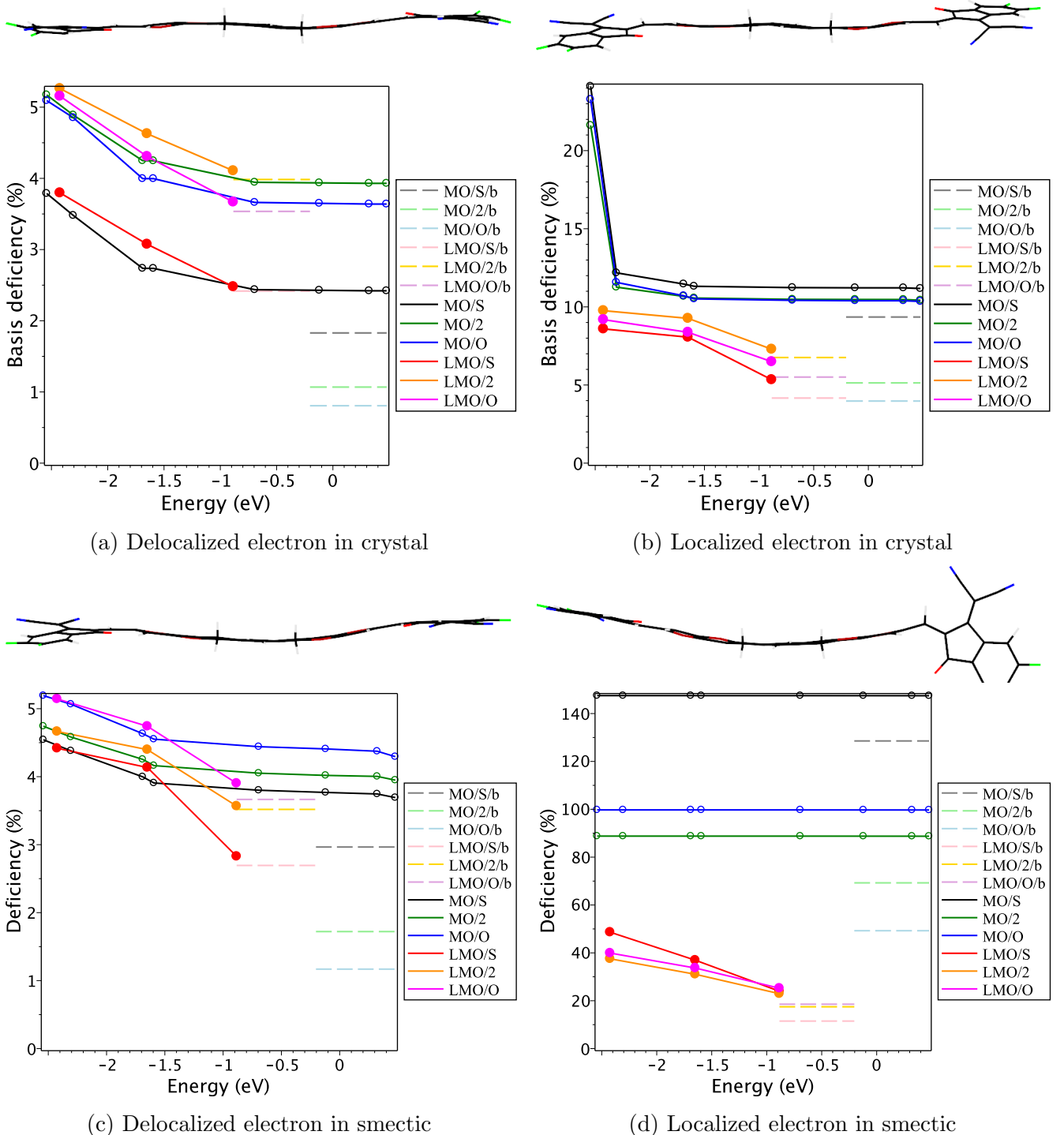


Figure S11: Detailed analysis of extreme cases of the dataset from Fig. S8 (strictly speaking, a subset of the first 100 configurations is used). The two extremes are when LUMO is fully delocalized across the molecule as LUMO in Fig. S3 or fully localized on one end as LMO1 in Fig. S4. In particular, in the panel (d) the wave-function is localized on the acceptor block which is rotated at around 90°. Each black dot counted from left to right corresponds to increase of the basis by one MO whose energy is marked on horizontal axis. The three red dots correspond to LMO basis of 2, 4 and 6 orbitals, whose highest energy is marked on the axis.

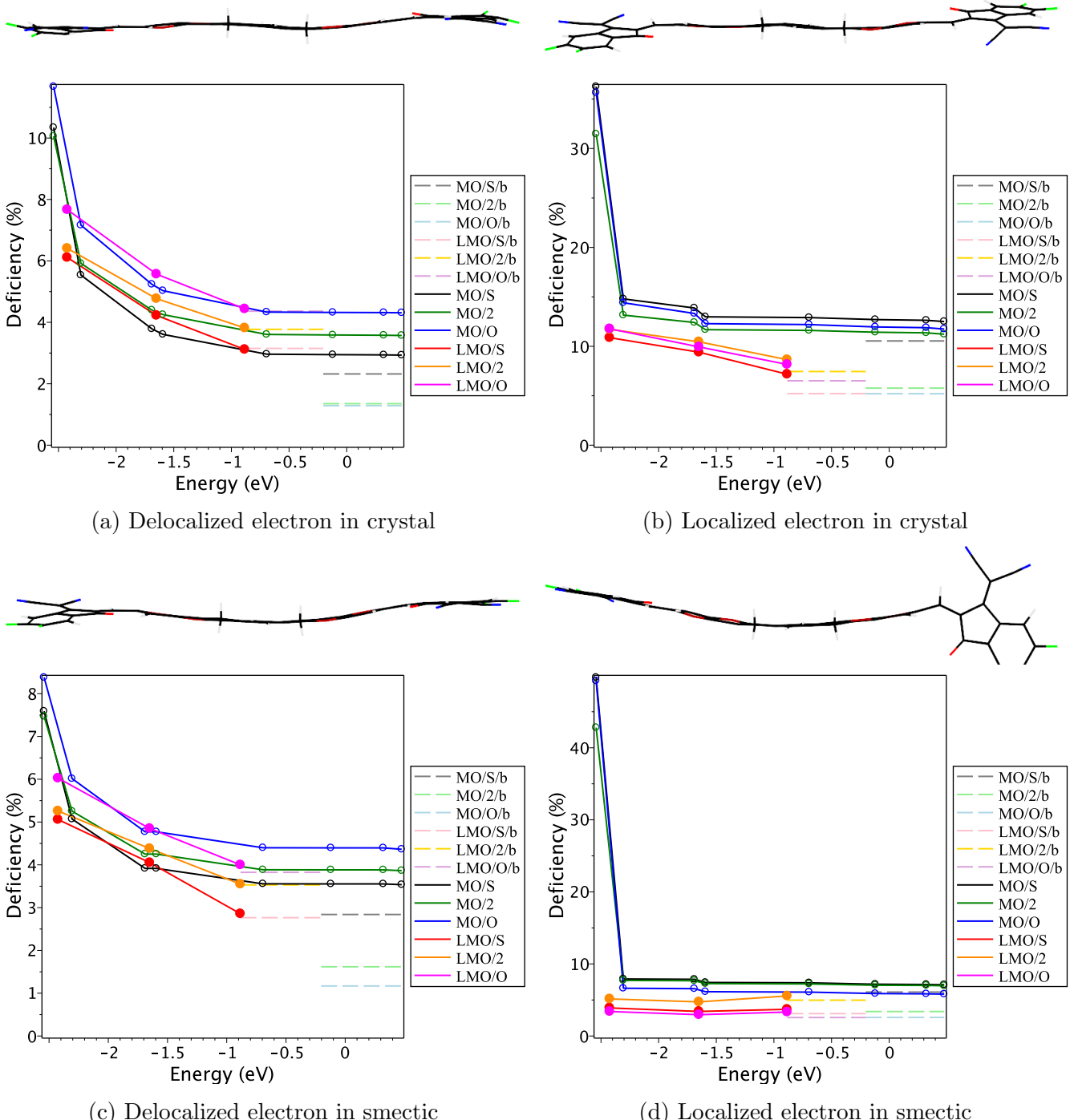
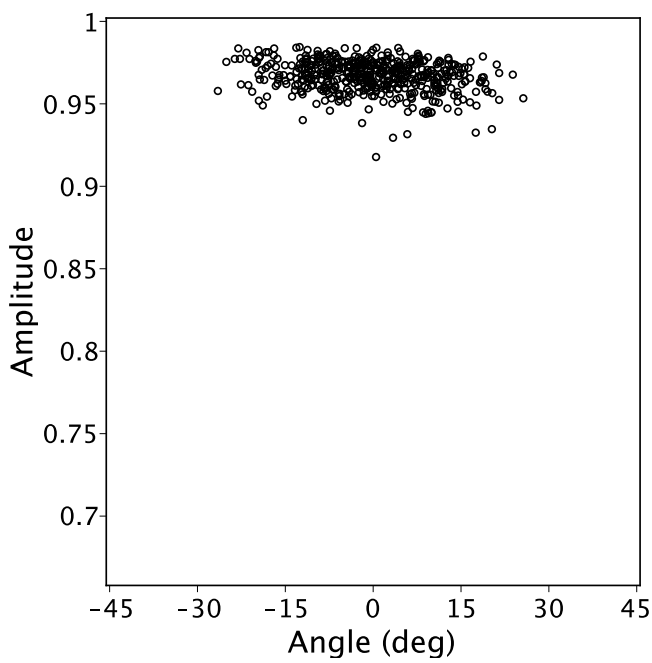
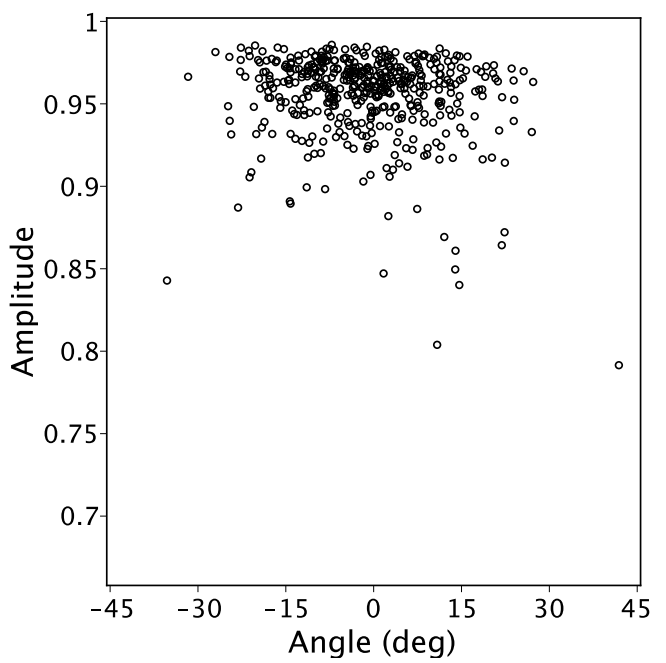


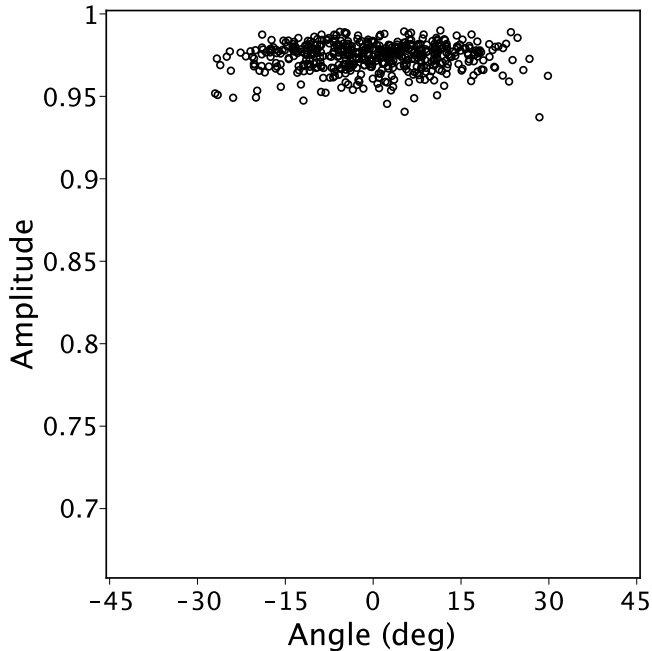
Figure S12: The same as Fig. S11 but with NO instead of MO. Note that in panel (d) the anion NO is localized on the opposite end (the left hand end) then LUMO in Fig. S11d.



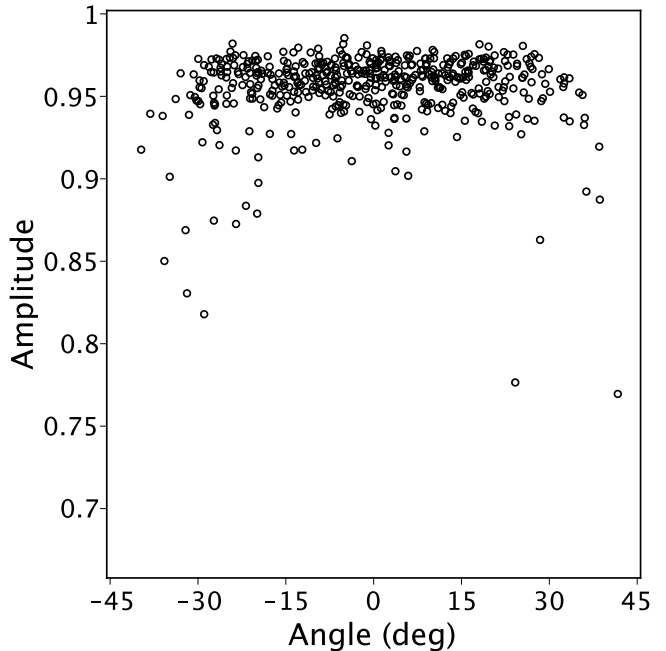
(a) Classical MD in crystal



(b) Classical MD in smectic

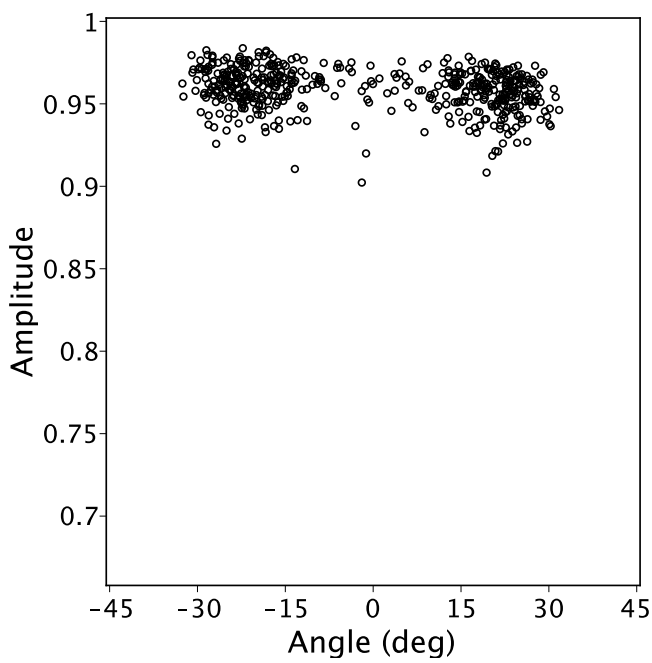


(c) Classical vibrations

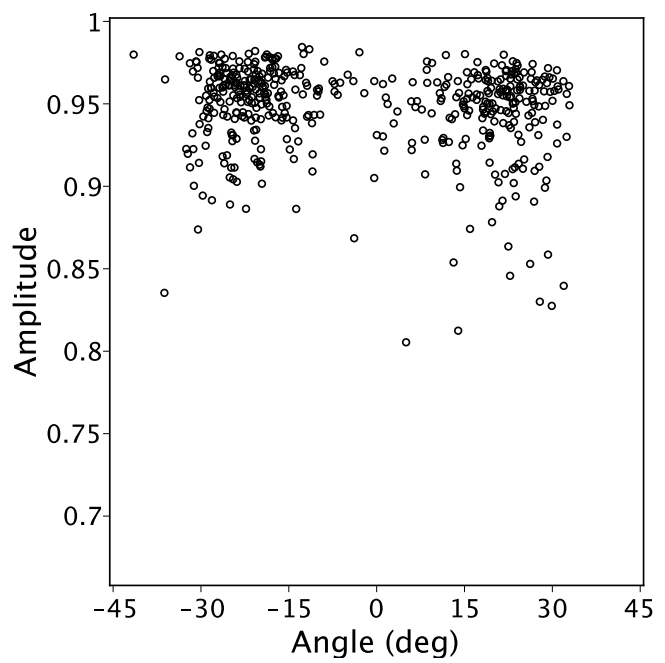


(d) Quantum vibrations

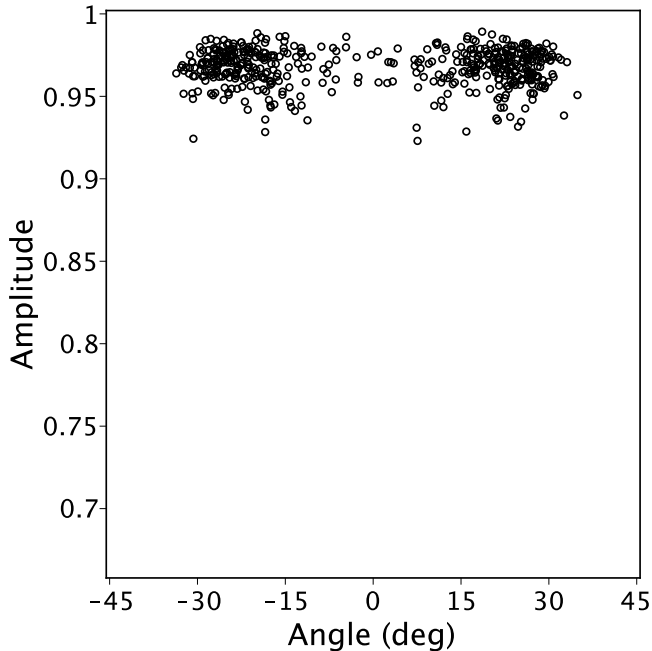
Figure S13: Coefficients of the expansion of LUMO of distorted molecules in two LMOs in polar representation rotated by  $45^\circ$ :  $c_1 = A \cos(\alpha + \pi/4)$  and  $c_2 = A \sin(\alpha + \pi/4)$ , where  $A$  is the amplitude and  $\alpha$  is the angle. In these notations,  $\alpha \approx \pm\pi/4$  corresponds to the wave-function localized on one of the two acceptors, whereas  $\alpha \approx 0$  corresponds to the delocalized wave-function; deviations of  $A$  from 1 mean deficiency of the basis of two orbitals.



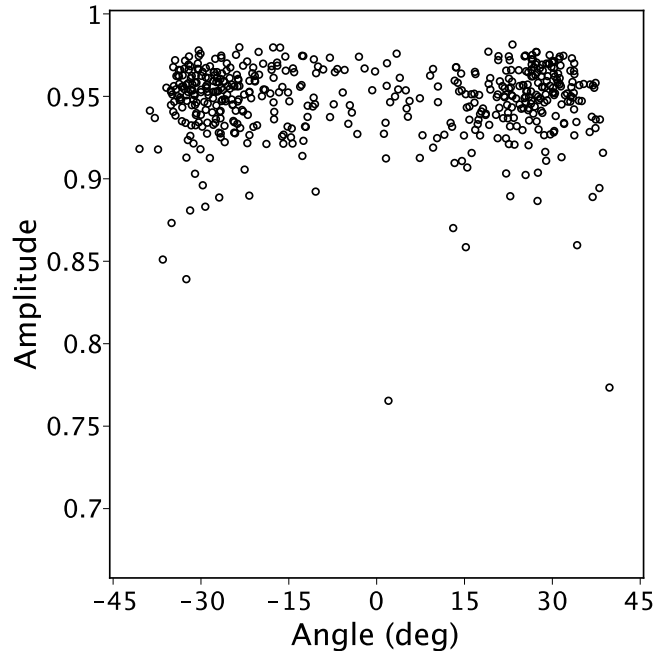
(a) Classical MD in crystal



(b) Classical MD in smectic

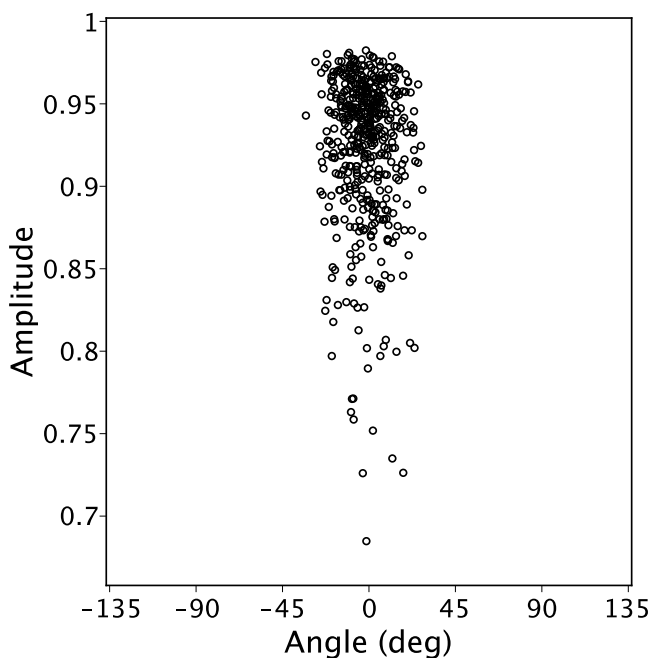


(c) Classical vibrations

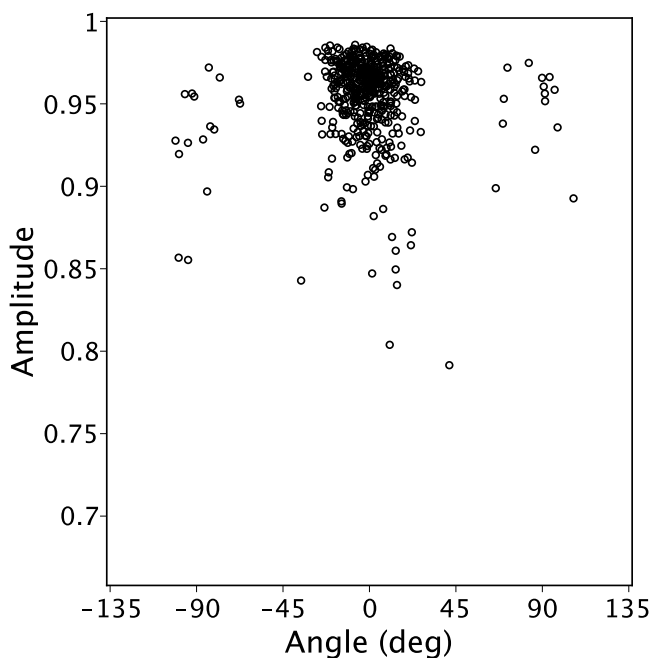


(d) Quantum vibrations

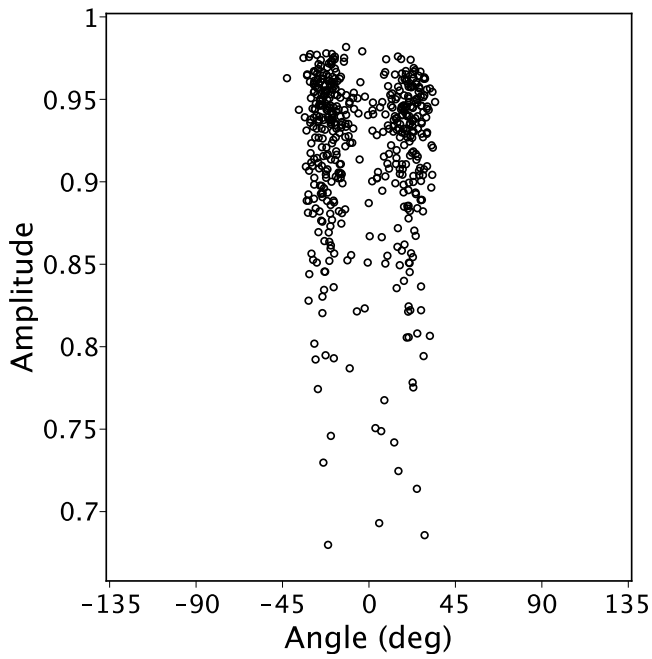
Figure S14: The same as Fig. S13 but with anion NO instead of LUMO.



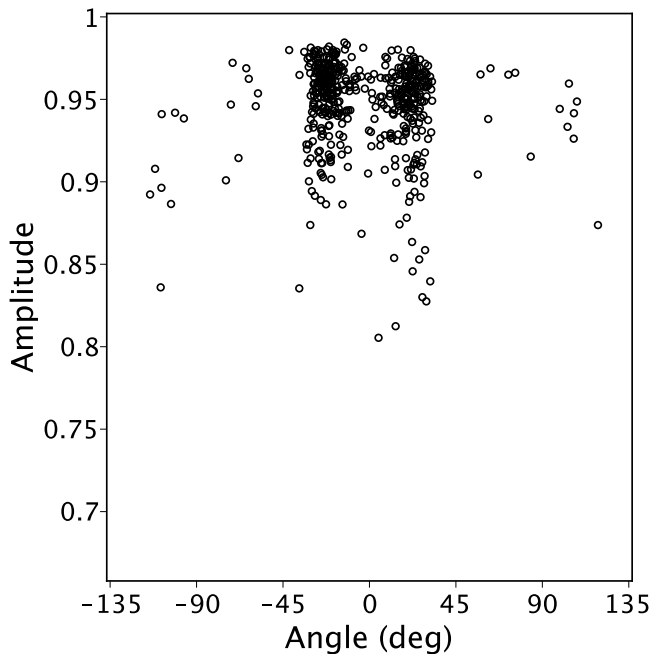
(a) Electron MO in smectic in CMO-basis



(b) Electron MO in smectic in LMO-basis

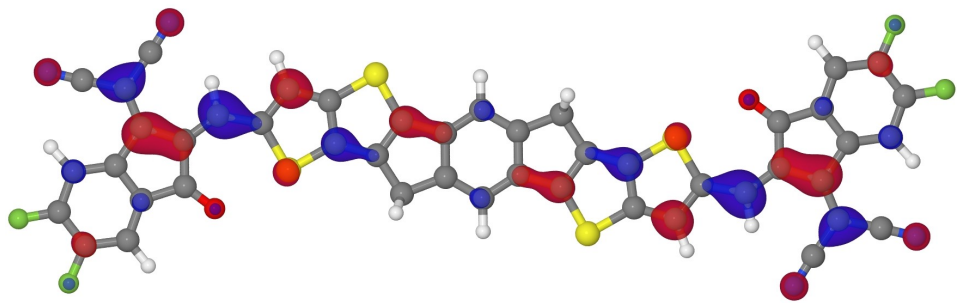


(c) Electron NO in smectic in CMO-basis

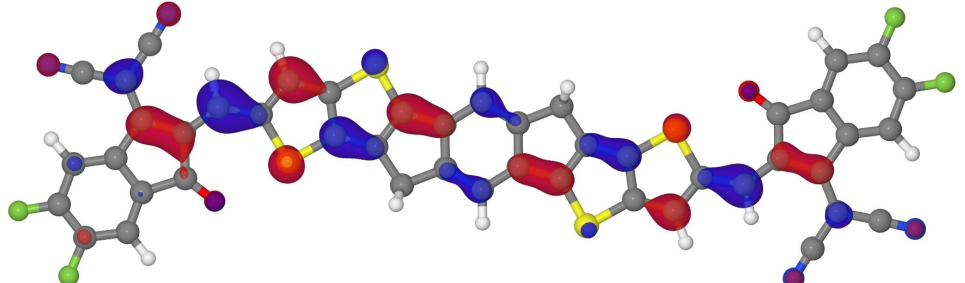


(d) Electron NO in smectic in LMO-basis

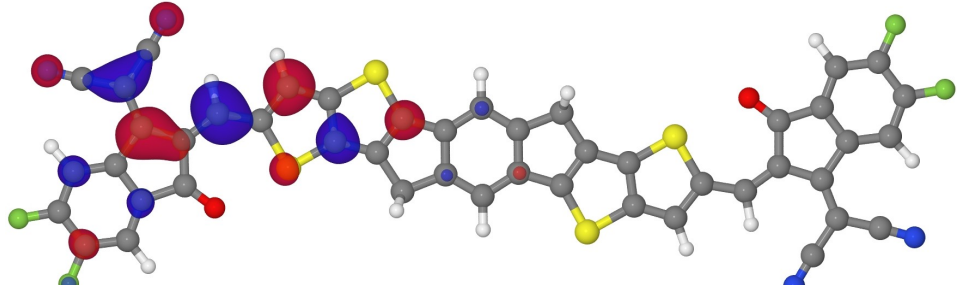
Figure S15: Molecular fluctuations sampled from MD of smectic are large enough to make basis of 2 LMOs and 2 LUMOs substantially different resulting in different expansion coefficients as visualized in these figures.



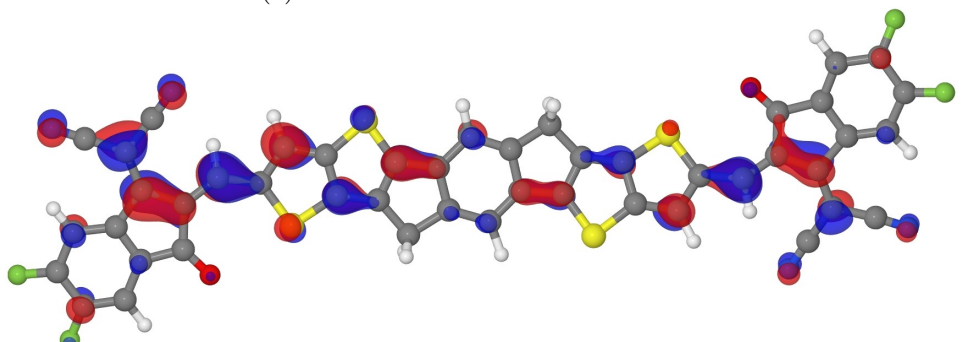
(a) LUMO



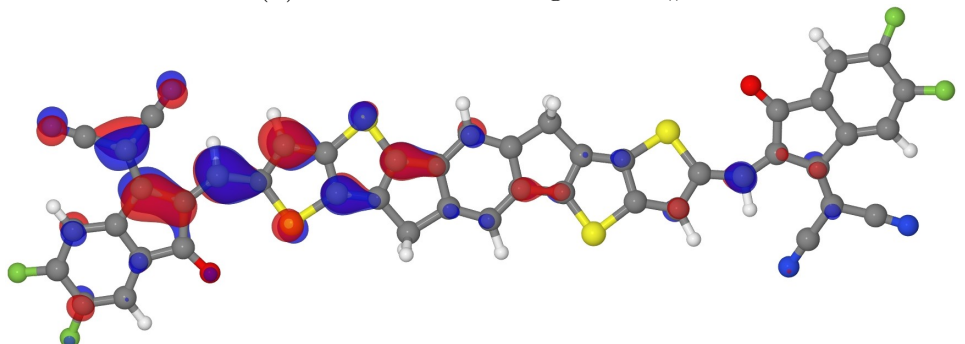
(b) Anion NO (in vacuum)



(c) Anion NO in water-like CPCM

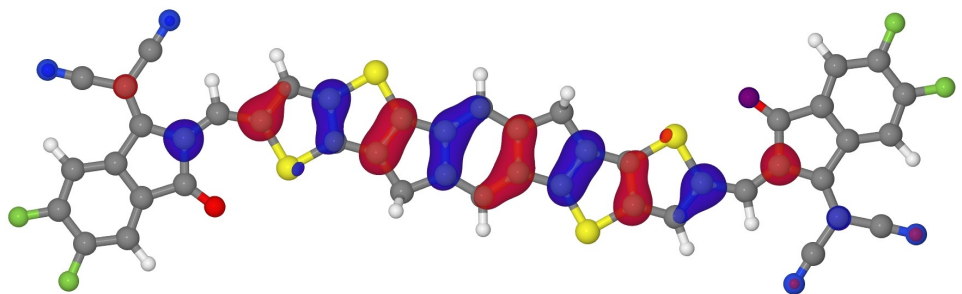


(d) LUMO of the configuration #2

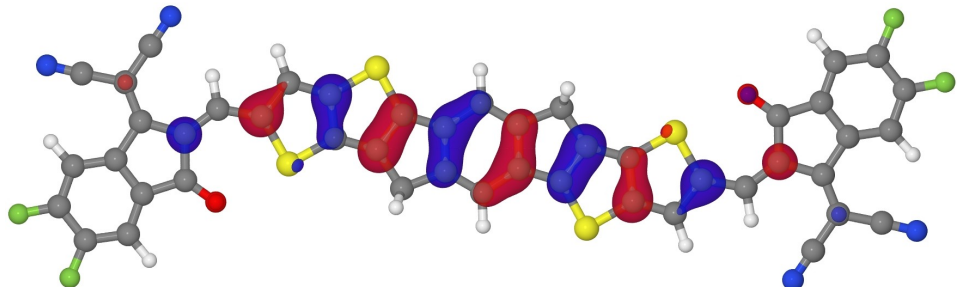


(e) Electron NO of the configuration #2

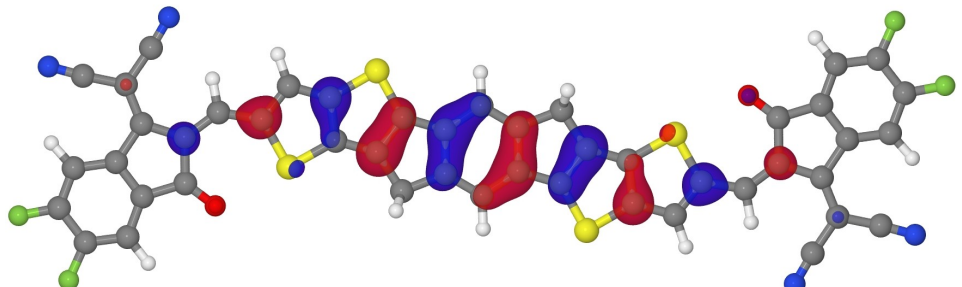
Figure S16: Localization of electron wave-function on one of the two acceptor blocks. It should be noted that even if the LUMO is delocalized as in the panel (d), the electron NO for the same geometry might be localized as in the panel (e).



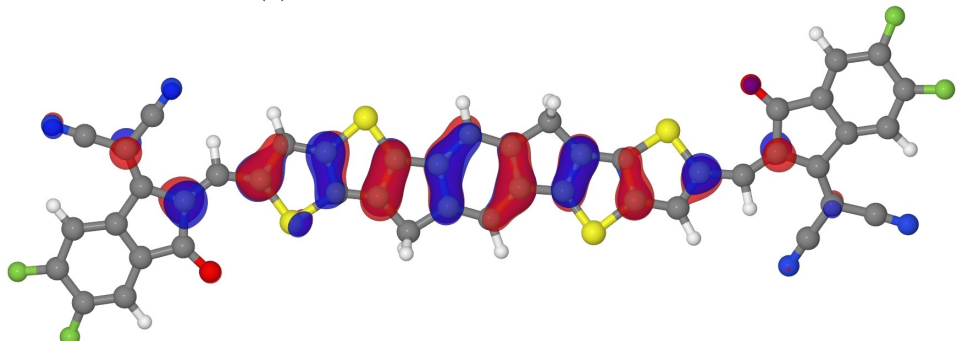
(a) HOMO



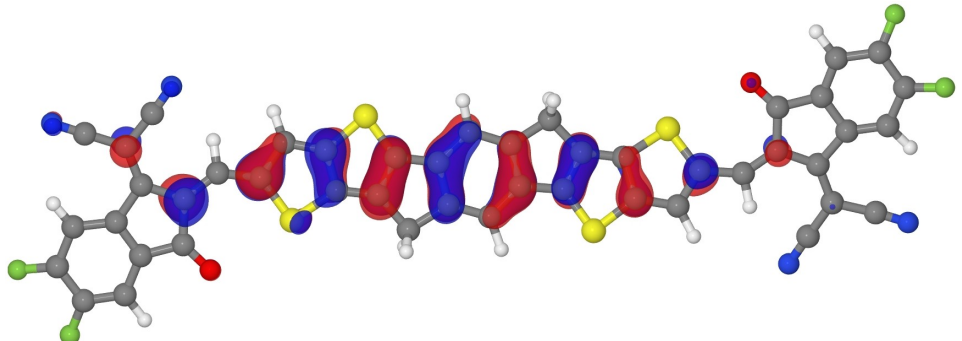
(b) Cation NO (in vacuum)



(c) Cation NO in water-like CPCM



(d) HOMO of the configuration #2



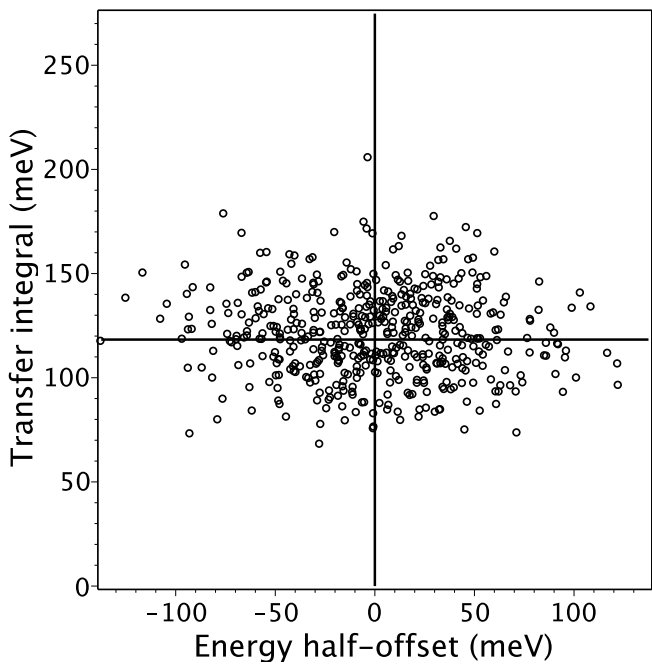
(e) Hole NO of the configuration #2

Figure S17: In contrast to electrons, hole NO is visually the same as HOMO (no localization because there is only one donor block).

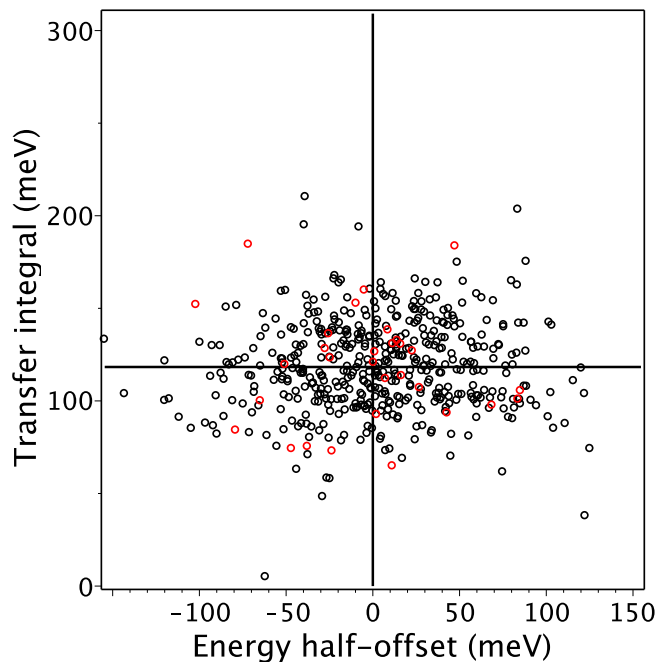
## S5 Fluctuations of tight-binding Hamiltonian

Table S10: Statistical analysis (500 conformations) of tight-binding Hamiltonian: mean value  $\langle \cdot \rangle$  and standard deviation  $\sigma(\cdot)$  for energy half-offset  $\epsilon = (\varepsilon_2 - \varepsilon_1)/2$  and transfer integral  $t$  between pair of LMOs (all in meV). For convenience of representation, all data values are multiplied by the sign of the reference value, which itself is calculated for the undistorted molecule. Since transfer integrals change their sign upon 180°-flip of  $\pi$ -conjugated blocks, the analysis is performed separately for main sign data subset (+) and minor sign subset (-), the size of the latter is given by  $N^-$ . To quantify the difference between classical and quantum vibrations, we can consider the displaced harmonic oscillator model of electronic transitions. In this model, onsite energy fluctuations are given by  $\sigma^2 = \sum_{\omega} S_{\omega} \hbar^2 \omega^2 \coth \frac{\hbar\omega}{2T}$  in the quantum treatment, whereas in classical approximation the  $\coth x$  is replaced by  $1/x$ ; here  $S_{\omega}$  is Huang–Rhys factor of vibrational mode  $\omega$ . From classical vibrations we can estimate the total reorganization energy  $\lambda = \sum_{\omega} S_{\omega} \hbar\omega \equiv \sigma_{\text{classical}}^2/(2T)$ , whereas the difference  $\sigma_{\text{quantum}}^2 - \sigma_{\text{classical}}^2$  can serve as a measure of importance of high-frequency modes ( $\hbar\omega \gg T$ ). Moreover, if we can separate low-frequency (LF) and high-frequency (HF) modes, we can differentiate impact of their fluctuations on electronic dynamics. Specifically in case of zero energy offset, the transfer rate between two electronic states is proportional to  $\exp(-\lambda_{\text{LF}}/4T - S_{\text{HF}}) \equiv \exp[-(\sigma_{\text{LF}}/2\sqrt{2}T)^2 - (\sigma_{\text{HF}}/\hbar\omega_{\text{HF}})^2]$ .

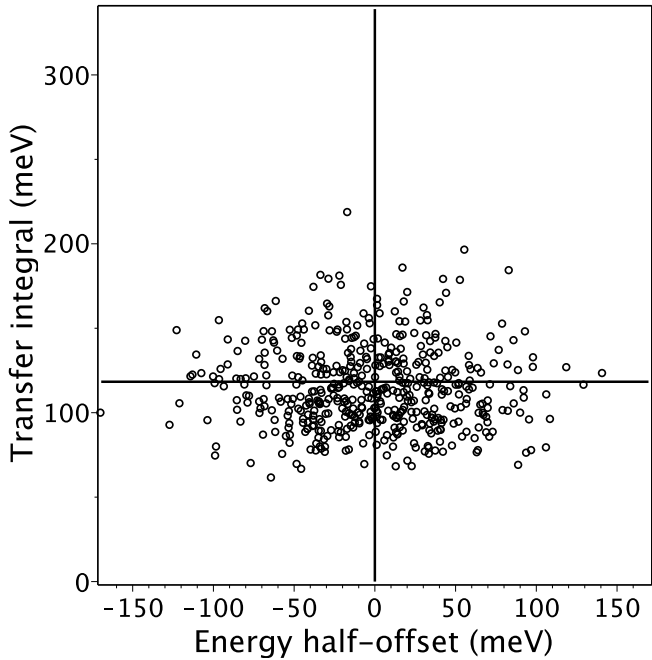
Data set	$\langle \epsilon \rangle$	$\sigma(\epsilon)$	$\langle t^+ \rangle$	$\sigma(t^+)$	$\langle t^- \rangle$	$\sigma(t^-)$	$N^-$
2-LMO model							
reference sign	+1		-1				
reference absolute value	0		118				
classical MD in crystal	0	(45)	121	(21)			
classical MD in smectic	3	(48)	118	(25)	-118	(30)	30
classical vibrations	-2	(48)	114	(25)			
quantum vibrations	2	(81)	114	(45)			
2 lowest LMOs in 6-LMO model							
classical MD in crystal	-2	(75)	63	(8)			
classical MD in smectic	0	(81)	62	(9)	-60	(13)	31
classical vibrations	5	(87)	70	(10)			
quantum vibrations	4	(150)	70	(16)			
2 lowest LMOs in block-diagonalized 6-LMO model							
classical MD in crystal	-2	(71)	80	(15)			
classical MD in smectic	0	(80)	78	(16)	-75	(19)	31
classical vibrations	5	(87)	67	(17)			
quantum vibrations	3	(148)	71	(29)			
Lowest acceptor-donor pair of LMOs in 6-LMO model							
reference sign	+1		-1				
reference absolute value	301		375				
classical MD in crystal	242	(76)	347	(24)			
classical MD in smectic	259	(82)	343	(29)	-316	(46)	15
classical vibrations	301	(87)	362	(33)			
quantum vibrations	292	(150)	360	(48)			
2 acceptor LMOs in 6-LMO model							
reference sign	+1		+1				
reference absolute value	338		0				
classical MD in crystal	344	(56)	67	(60)			
classical MD in smectic	350	(54)	67	(67)			
classical vibrations	330	(60)	-12	(70)			
quantum vibrations	326	(96)	5	(113)			
2 donor LMOs in 6-LMO model							
reference sign	+1		+1				
reference absolute value	258		0				
classical MD in crystal	253	(38)	-7	(65)			
classical MD in smectic	270	(38)	-4	(73)			
classical vibrations	254	(41)	2	(75)			
quantum vibrations	247	(78)	-4	(120)			



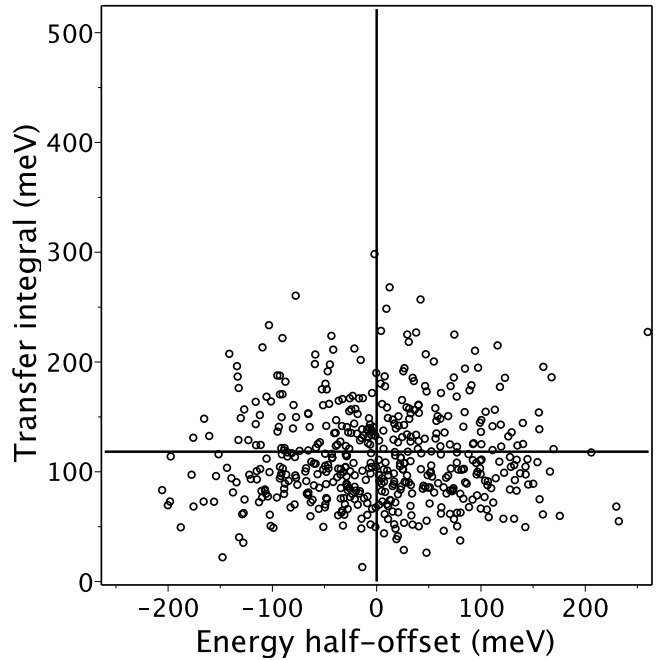
(a) Classical MD in crystal



(b) Classical MD in smectic

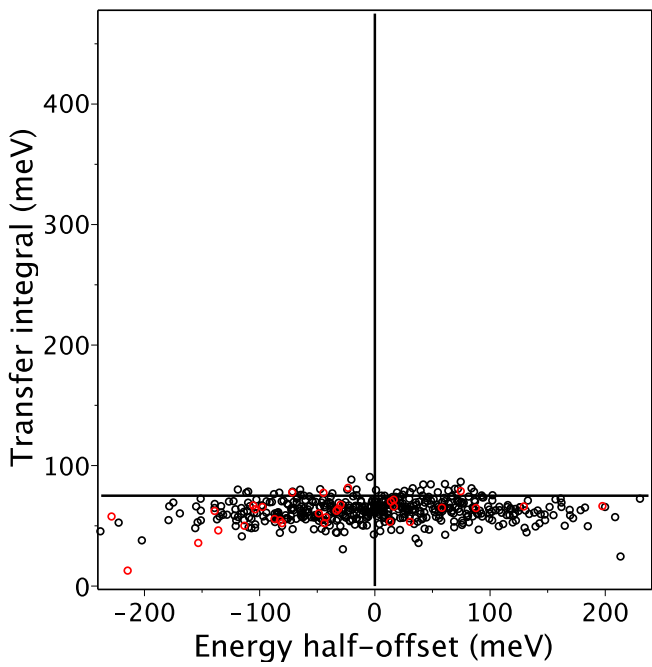


(c) Classical vibrations

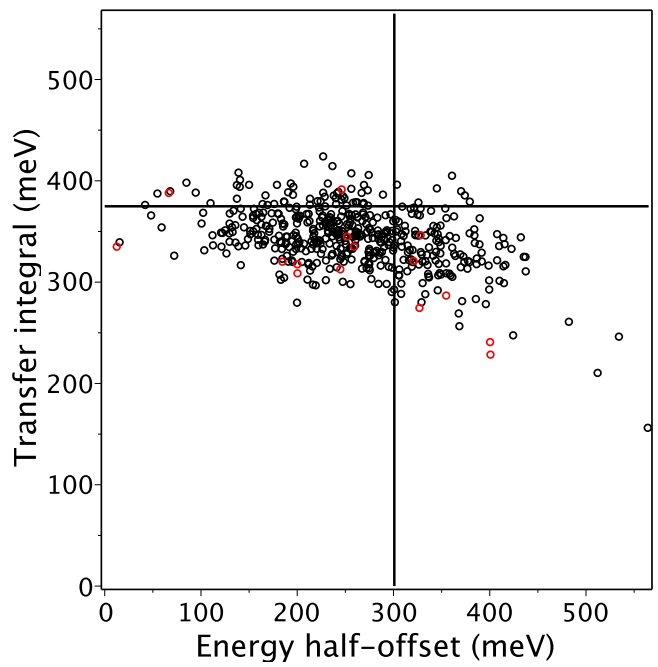


(d) Quantum vibrations

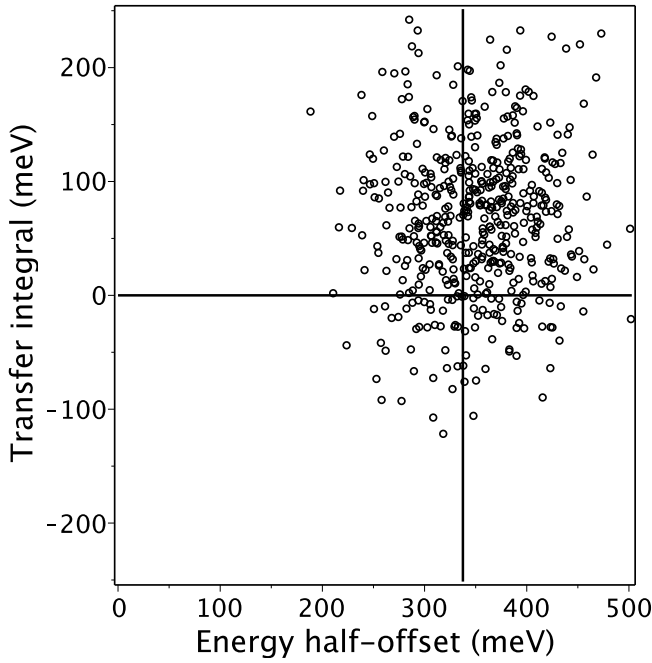
Figure S18: Fluctuations of half-energy offset and transfer integral in 2-LMO tight-binding model. Scales of horizontal and vertical axes are made equal. Red dots show negative values taken with opposite sign.



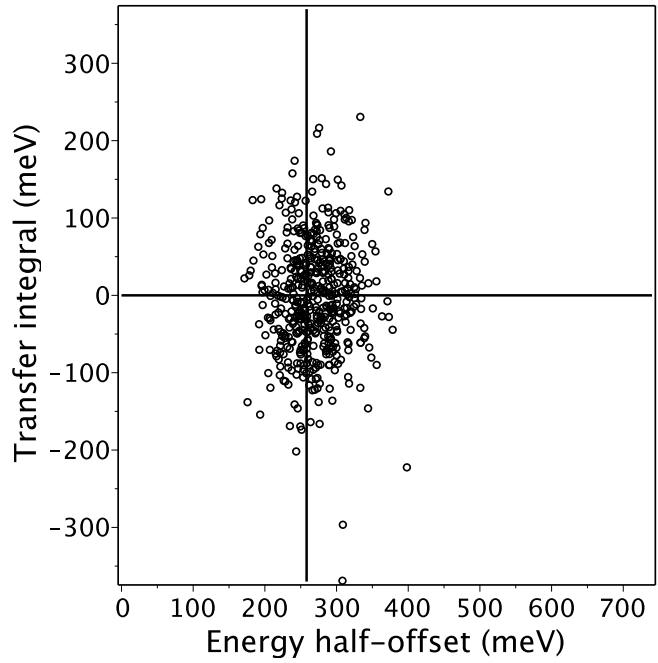
(a) Acceptor-acceptor through donor



(b) Acceptor-donor

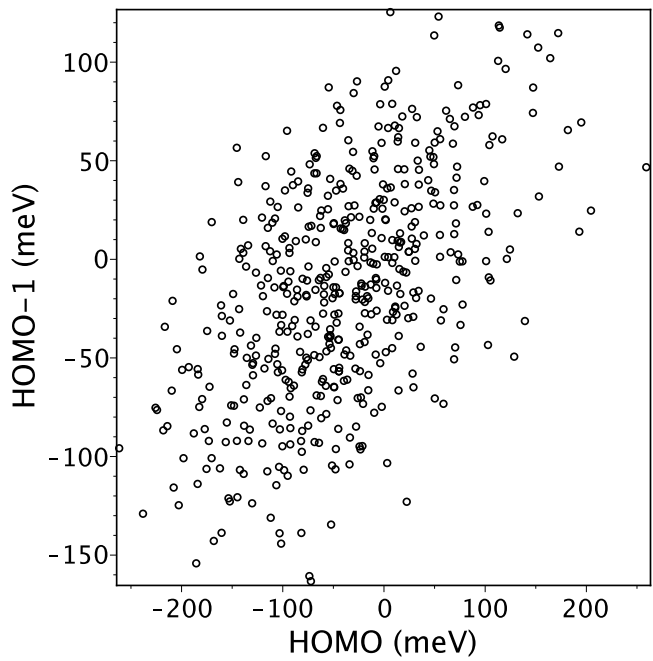


(c) Acceptor intra-block

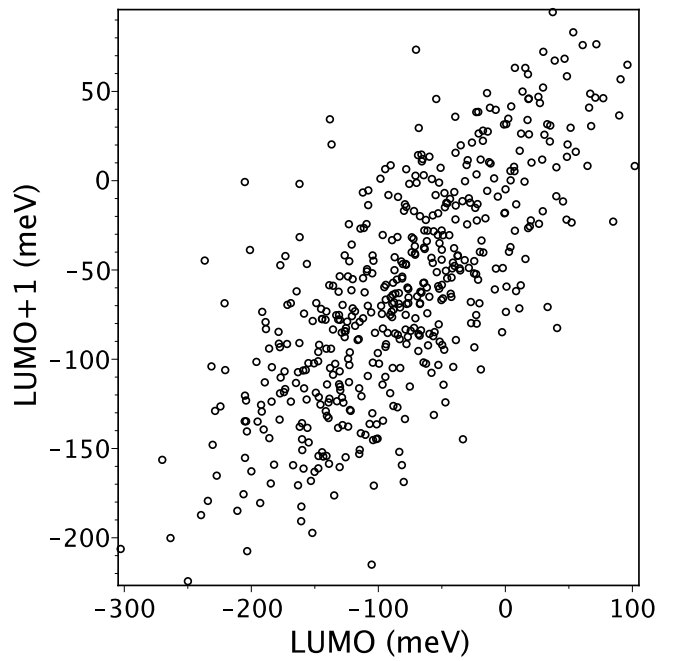


(d) Donor intra-block

Figure S19: Fluctuations of half-energy offset and transfer integral for different pairs of LMOs in 6-LMO tight-binding model of the smectic data set. Lowest possible LMOs are used (there are two LMOs per block). Scales of horizontal and vertical axes are made equal. Red dots show negative values taken with opposite sign.



(a) Occupied



(b) Unoccupied

Figure S20: Fluctuations of energy of frontier MOs for the smectic data set relative to the reference values which are calculated for the undistorted molecule. In particular, the reference HOMO/HOMO-1 gap is 800 meV and LUMO/LUMO+1 gap is 237 meV.

## S6 Impact on charge transport parameters

Table S11: Impact on charge transport parameters. Three topologies of electronic connectivity are considered: 1D slipstack, 2D brickwork, 3D wiremesh, see Figs. S21 and S22 for notations. Here  $t_0$  is the intramolecular coupling and  $t_{1,2}$  are intermolecular ones. The ‘error’ column shows the error of the 1-site approximation (sites connected via  $t_0$  are merged), relative to the ‘full model’ which is 2-site model (all sites shown in Figs. S21 and S22 are taken into account). To simplify formulas in 2D and 3D, two limiting cases are considered: of equal couplings and when  $t_0$  is large. For wiremesh,  $a_{1,2,3}$  denote  $a, b, c$ . “Full model” formulas are derived in Ref.[TB] as ‘honeycomb’ and ‘K4o’ lattices, 1-site model can be obtained by taking limit  $t_0 \rightarrow \infty$ , rescaling  $t_{1,2}$  by a factor of 1/2 (as explained in the main text), and rescaling hopping rates by a factor of 2 to correctly describe the transformation from two merged sites to a single site.

topology	parameters	Inverse mass		Hopping amplitude	
		full model	error	full model	error
slipstack	–	$m^{-1} = a^2 \frac{t_0 t_1}{t_0 + t_1}$	$\frac{1 + t_1/t_0}{2}$	$\eta^2 = \frac{a^2}{2} \frac{t_0^2 t_1^2}{t_0^2 + t_1^2}$	$\frac{1 + t_1^2/t_0^2}{2}$
brickwork	$t_{0,1,2} = t$ $a = b$ $\gamma = 120^\circ$	$m_{1,2}^{-1} = \frac{1}{2} a^2 t$	$\frac{3}{2}, \frac{1}{2}$	$\eta_{1,2}^2 = \frac{1}{4} a^2 t^2$	$\frac{3}{2}, \frac{1}{2}$
brickwork	$t_{1,2} \ll t_0$	$\frac{1}{m_1} + \frac{1}{m_2} = a^2 t_1 + b^2 t_2$ $\frac{1}{m_1 m_2} =  \mathbf{a} \times \mathbf{b} ^2 t_1 t_2$	$\frac{1}{2}, \frac{1}{2}$	$\eta_1^2 + \eta_2^2 = \frac{1}{2} (a^2 t_1^2 + b^2 t_2^2)$ $\eta_1 \eta_2 = \frac{1}{2}  \mathbf{a} \times \mathbf{b} ^2 t_1 t_2$	$\frac{1}{2}, \frac{1}{2}$
wiremesh	$t_{0,1,2} = t$	$m_i^{-1} = \frac{1}{8} a_i^2 t, i = \overline{1,3}$	$1, 1, \frac{1}{2}$	$\eta_i^2 = \frac{1}{16} a_i^2 t^2, i = \overline{1,3}$	$1, 1, \frac{1}{2}$
wiremesh	$t_{1,2} \ll t_0$	$m_i^{-1} = \frac{1}{4} a_i^2 t_i, i = \overline{1,2}$ $m_3^{-1} = \frac{1}{4} a_3^2 \frac{t_1 t_2}{t_1 + t_2}$	$\frac{1}{2}, \frac{1}{2}, \frac{1}{2}$	$\eta_i^2 = \frac{1}{8} a_i^2 t_i^2, i = \overline{1,2}$ $\eta_3^2 = \frac{1}{8} a_3^2 \frac{t_1^2 t_2^2}{t_1^2 + t_2^2}$	$\frac{1}{2}, \frac{1}{2}, \frac{1}{2}$

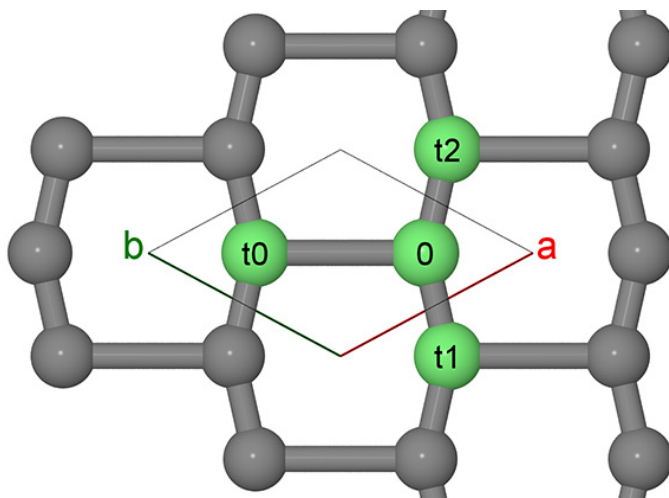


Figure S21: Brickwork lattice topology and electronic couplings to site ‘0’. Site/bond percolation threshold is 0.697/0.653 [Tran13].

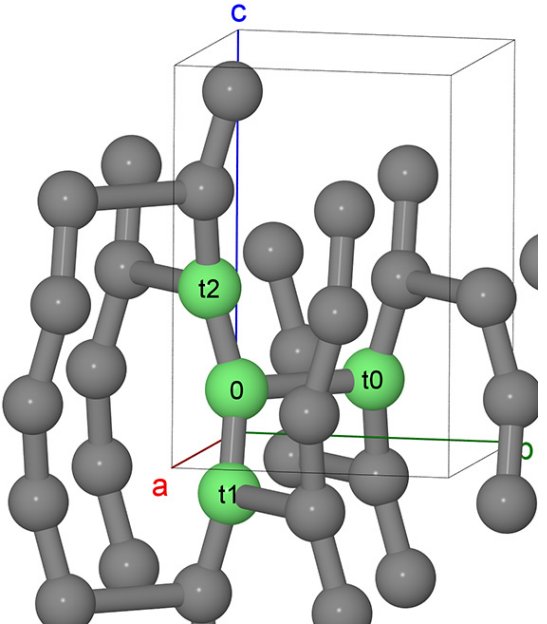


Figure S22: Wiremesh lattice topology and electronic couplings to site ‘0’. Site/bond percolation threshold is 0.571/0.551 [Tran13].

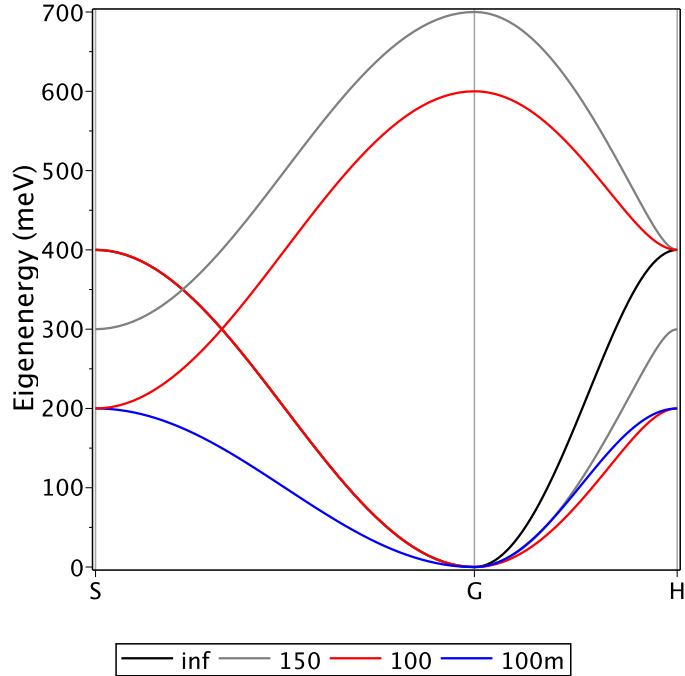


Figure S23: Electronic band structure of the brickwork lattice (Fig. S21) with  $t_1 = t_2$ : comparison of four different models. Here in a series of models ‘100’, ‘150’, ‘inf’,  $t_1 = 100$  meV and  $t_0$  is increased from 100 meV to infinity. In model ‘100m’ the two intramolecular sites are merged so that  $t_1 = 50$  meV and  $t_0 = \infty$ . The k-points ‘S’=(1/2,1/2) and ‘H’=(1/2,-1/2), so that k-paths ‘GS’ and ‘GH’ correspond to perpendicular and parallel directions with respect to the long axis of the molecule. The dispersion of the lowest branch along ‘GS’ path does not depend on  $t_0$  so that the three curves with  $t_1 = 100$  meV collapse to a single curve crossing ‘S’-point at 400 meV. The upper subband is absent for  $t_0 = \infty$  (it is infinitely separated). The crossing between the two subbands via Dirac cone is moving from k-point (1/3,1/3) for  $t_0 = t_1$  to (1/2,1/2) for  $t_0 = 2t_1$ , so that for  $t_0 > t_1 + t_2$  the subbands are disconnected. Comparison of effective masses of 2-site (‘100’) and 1-site (‘100m’) models shows that by merging the two sites we introduce an artificial anisotropy: effective mass increases along ‘GS’ and decreases along ‘GH’ k-paths.

## References

- [Gaussian] Gaussian 16, Revision A.03, M. J. Frisch *et al*, Gaussian, Inc., Wallingford CT (2016)
- [GROMACS] M Abraham, T Murtola, R Schulz, S Pall, J Smith, B Hess, E Lindahl, GROMACS: High performance molecular simulations through multi-level parallelism from laptops to supercomputers, SoftwareX 1-2, 19 (2015)
- [LMO] Electronic coarse-graining of insulators, <http://zhugayevych.me/CMS/protocols.html#ecg>
- [MolMod] MolMod – open-source Molecular Modeling package, <http://zhugayevych.me/maple/MolMod>
- [TB] Tight-binding models, <http://zhugayevych.me/CMS/TB.html>
- [Tran13] J Tran, T Yoo, S Stahlheber, A Small, Percolation thresholds on three-dimensional lattices with three nearest neighbors, J Stat Mech Theor Exp 2013, P05014 (2013)
- [Tukachev19] N V Tukachev, D R Maslenikov, A Y Sosorev, S Tretiak, A Zhugayevych, Ground state geometry and vibrations of polyphenylenevinylene oligomers, J Phys Chem Lett 10, 3232 (2019)
- [Zhugayevych16] A Zhugayevych, O Postupna, H L Wang, S Tretiak, Modification of optoelectronic properties of conjugated oligomers due to donor/acceptor functionalization: DFT study, Chem Phys 481, 133 (2016)
- [Zhugayevych18] A Zhugayevych, O Mazaleva, A Naumov, S Tretiak, Lowest-energy crystalline polymorphs of P3HT, J Phys Chem C 122, 9141 (2018)